



Centimeter-scale mapping of phototrophic biofilms in glacial forefields using visible band ratios and UAV imagery

Matteo Roncoroni, Davide Mancini, Tyler J. Kohler, Floreana Miesen, Mattia Gianini, Tom J. Battin & Stuart N. Lane

To cite this article: Matteo Roncoroni, Davide Mancini, Tyler J. Kohler, Floreana Miesen, Mattia Gianini, Tom J. Battin & Stuart N. Lane (2022): Centimeter-scale mapping of phototrophic biofilms in glacial forefields using visible band ratios and UAV imagery, International Journal of Remote Sensing, DOI: [10.1080/01431161.2022.2079963](https://doi.org/10.1080/01431161.2022.2079963)

To link to this article: <https://doi.org/10.1080/01431161.2022.2079963>



© 2022 The Author(s). Published by Informa UK Limited, trading as Taylor & Francis Group.



[View supplementary material](#)



Published online: 15 Jun 2022.



[Submit your article to this journal](#)



[View related articles](#)



[View Crossmark data](#)

Centimeter-scale mapping of phototrophic biofilms in glacial forefields using visible band ratios and UAV imagery

Matteo Roncoroni ^a, Davide Mancini ^a, Tyler J. Kohler ^b, Floreana Miesen^a, Mattia Gianini^a, Tom J. Battin^b and Stuart N. Lane ^a

^aInstitute of Earth Surface Dynamics, University of Lausanne, UNIL Mouline, Lausanne, Switzerland; ^bRiver Ecosystems Laboratory, Alpine and Polar Environmental Research Center Ecole Polytechnique Fédérale de Lausanne (EPFL), Lausanne, Switzerland

ABSTRACT

Microbial biofilms have received great attention in the last few decades from both aquatic ecologists and biogeomorphologists. Most recently, this has focused on mapping biofilms to understand their spatial distributions and ecosystem services. Such studies often involve the use of satellite imagery, which typically provides large temporal and spatial scales and wide-range spectral information. Although satellites have the advantage of multi- and hyper-spectral sensors, images often have low spatial resolution that limits their use in river studies, where both rivers are narrower and stream processes occur at resolutions smaller than the footprint of satellite sensors. Spatial resolution is sensor quality dependent but also controlled by sensor elevation above the ground. Hence, high resolutions can be achieved either by using a very expensive sensor or by decreasing the distance between the target area and the sensor itself. To date, sensor technology has advanced to a point where multi- or even hyper-spectral cameras can be easily carried out by an Uncrewed Aerial Vehicle (UAV) at unprecedented spatial resolutions. Where such sensors have high spectral resolution, they are often prohibitively expensive, especially as their use in extreme environments such as glacial forefields risks UAV damage. In this paper, we test the performance of visible band ratios in mapping biofilms in an Alpine glacier forefield characterized by a well-developed and heterogeneous stream ecosystem but using a low-cost UAV. The paper shows that low-cost and consumer grade UAVs can be easily deployed in such extreme environments, delivering both quality RGB images for photogrammetric (SfM-MVS) processing and sufficient spectral information for benthic biofilm mapping at high temporal and spatial resolution.

HIGHLIGHTS

- RGB cameras are an alternative to expensive multi- or hyper-spectral cameras.
- Phototrophic biofilms can be detected and mapped through visible band ratios.
- High-temporal and high-resolution imagery can be collected by consumer-grade UAVs.
- Biofilm presence is restricted to stable and water-fed terraces in summer.


ARTICLE HISTORY

Received 16 March 2022
Accepted 12 May 2022

KEYWORDS

Stream biofilm mapping; UAV; SfM-MVS photogrammetry; visible-Band-Ratios; remote sensing

CONTACT Matteo Roncoroni  matteo.roncoroni@unil.ch  Institute of Earth Surface Dynamics, University of Lausanne, UNIL Mouline, 1015 Lausanne, Switzerland

 Supplemental data for this article can be accessed online at <https://doi.org/10.1080/01431161.2022.2079963>

© 2022 The Author(s). Published by Informa UK Limited, trading as Taylor & Francis Group.

This is an Open Access article distributed under the terms of the Creative Commons Attribution-NonCommercial-NoDerivatives License (<http://creativecommons.org/licenses/by-nc-nd/4.0/>), which permits non-commercial re-use, distribution, and reproduction in any medium, provided the original work is properly cited, and is not altered, transformed, or built upon in any way.

1. Introduction

Biofilms are surface-attached microbial communities (Costerton et al., 1995) encapsulated in an extracellular polymeric matrix (Flemming and Wingender, 2010). The biofilm mode of life has been shown to be ubiquitous and highly adapted to primary colonization in aquatic environments (Flemming and Wuertz, 2019). In streams and rivers, benthic biofilms are involved in ecosystem processes (Battin et al., 2003, 2016) including nutrient uptake and recycling and carbon fluxes, and serve as the base of the food web. Biofilms may also stabilize fine sediments (Neumeier et al., 2006; Gerbersdorf et al., 2009; Fang et al., 2014; Gerbersdorf and Wieprecht, 2015), even at large spatial scales (e.g. in estuaries; Brückner et al., 2021), thereby reducing vertical infiltration and supporting plant development in water-stressed environments (Miller and Lane, 2019; Roncoroni et al., 2019). Accordingly, several papers have argued that benthic biofilms should be included in the list of ecosystem engineers (*sensu* Jones et al., 1994) due to their capacity for modifying the physical state of biotic and/or abiotic materials for the benefit of other organisms (Gerbersdorf et al., 2008; Gerbersdorf et al., 2009; Roncoroni et al., 2019).

In recent years, research has mapped benthic biofilms to understand their spatial distributions (e.g. Méléder et al., 2003) and/or to determine their biomass (e.g. Combe et al., 2005). This is often possible due to the different spectral signatures of benthic biofilms, including photosynthetically active pigments (e.g. chlorophyll-*a*), compared to uncolonized substrates (Benyoucef et al., 2014; Salvatore et al., 2020). Such studies usually involve satellite or airborne imagery, which is excellent for large spatial scales and can provide a wide range of spectral information (e.g. by using multi- and hyper-spectral sensors).

For example, Méléder et al. (2003) mapped the presence of benthic biofilms for Bourgneuf Bay (France) between 1986 and 1998 with the Normalized Difference Vegetation Index (NDVI; Tucker, 1979) calculated from multi-spectral satellite imagery. The authors found that biofilms had a specific NDVI range that allows discrimination from the uncolonized substrata but also from macro-algae. In the same way, Benyoucef et al. (2014) investigated the inter-annual distribution of benthic biofilms in the Loire estuary (France) between 1991 and 2009 and found that the NDVI derived from multi-spectral imagery was efficient for mapping purposes at the large scale. Both studies reported that the spatial resolution of their imagery (typically 20 × 20 m) was too coarse to measure high-resolution spatial variations in biofilm distribution, which may extend down to the centimetre-scale (Méléder et al., 2003; Benyoucef et al., 2014). More recently, Salvatore et al. (2020) and Power et al. (2020) used high-resolution satellite-based NDVI to identify the inter-annual and intra-seasonal distribution of photosynthetically active biofilms in the Fryxell basin, Antarctica. Both studies confirmed the efficiency of the NDVI in mapping biofilms, and Power et al. (2020) went even further by estimating the microbial mat biomass of the Fryxell basin.

Combe et al. (2005) estimated biofilm biomass and mapped biofilm distribution within Bourgneuf Bay using airborne hyper-spectral imagery. These authors found that this produced more reliable results than the multi-spectral imagery used by Méléder et al. (2003), primarily due to the increased spectral resolution of the sensor. Kazemipour et al. (2012) and Launeau et al. (2018) used hyper-spectral data to discriminate the main assemblages of benthic biofilms (e.g. diatom, cyanobacteria, etc.), and their biomass,

from the hyper-spectral datasets of Bourgneuf Bay. In both studies, discrimination was possible due to prior knowledge of the spectral response of the key biofilm assemblages (Kazemipour et al., 2012; Launeau et al., 2018).

The use of airborne sensors in the previous studies, rather than satellites, produced high spatial resolution datasets ranging from 5×5 m in Combe et al. (2005) to 0.7×0.7 m in Launeau et al. (2018). However, such spatial resolutions were at the expense of temporal ones, and in Combe et al. (2005), Kazemipour et al. (2012) and Launeau et al. (2018), the study zones were imaged only once or twice. In the presence of sharp environmental gradients, a higher spatial resolution may be a critical requirement. Indeed, higher resolution datasets, although sometimes more limited in spatial extent, may reduce the occurrence of spectral mixing (see Bioucas-Dias et al., 2013) and improve mapping accuracy and precision.

In stream studies, there is the need for sub-metre resolution datasets to appreciate stream processes (e.g. Carbonneau et al., 2004; Marcus and Fonstad, 2008; Woodget et al., 2015; Woodget and Austrums, 2017). Here, habitat gradients can occur over just a few centimetres to metres such as in actively braiding rivers. Here, the environments most conducive to biofilm development are commonly more stable secondary channels that may be only a few metres or less in width. Therein, centimetre-resolution data may be desirable and/or necessary because abiotic or biotic features can occur in or vary within very few centimetres of the channel.

Although spatial resolution is typically sensor-quality dependent, it is also controlled by the difference in elevation between the sensor and the ground (Westoby et al., 2012). Hence, high spatial resolution can be achieved either by using a very expensive sensor like those on board satellites/aircrafts or by decreasing the distance between the target area and the sensor itself. To date, sensor technology has advanced to a point where miniaturized multi- or even hyper-spectral surveys may be carried out by an uncrewed aerial vehicle (UAV), yielding wide-ranging spectral information at unprecedented spatial and temporal resolutions. For instance, (Harrison et al. 2020) used an UAV to collect hyper-spectral information for a 275-m-long reach of the American River in California (USA) and, amongst other techniques, used a biofilm-related chlorophyll-*a* map at 0.15 m resolution as a proxy to detect fall-run Chinook salmon (*Oncorhynchus tshawytscha*) spawning grounds. To our knowledge, benthic biofilm distribution and/or biomass has never been estimated from UAV-based multi-spectral imagery, and studies involving those sensors have focused upon algal bloom studies (see Kislik et al., 2018), trophic state monitoring (Su and Chou 2015), and aquatic vegetation mapping (Chabot et al., 2018; Song and Park, 2020; Taddia et al., 2020).

In this study, we assess the extent to which low-cost UAVs with integrated RGB cameras can be a cost-effective alternative to multi- or hyper-spectral devices in mapping benthic biofilm distributions in extreme environments such as glacial forefields where very high (cm) spatial and high (daily to weekly) temporal resolution is required. Although RGB sensors have a very low spectral resolution (the three visible bands, namely, red, green and blue), it should be possible to map benthic biofilms in shallow and clear channels based on these bands as compared to the un-colonized substrata (Benyoucef et al., 2014). This is partially confirmed by the studies of Xu et al. (2018) who were able to map green algal tides with visible band ratios, Flynn and Chapra (2014) who mapped submerged vegetation with statistical analysis of RGB images, and by Kislik et al. (2020) that mapped

filamentous algae by applying a supervised classification to their RGB images. The use of low-cost UAVs allows the costs of repeated mapping to be lowered and the financial consequences of sensor loss to be reduced.

We test the use of UAV-based and high-frequency RGB image acquisition with Structure-from-Motion Multiview-Stereo (SfM-MVS) photogrammetry (Westoby et al., 2012; Fonstad et al., 2013; Tamminga et al., 2015; Woodget et al., 2015; James et al., 2017, 2020; Dietrich, 2017; Roncoroni and Lane, 2019; Lane et al., 2020) to generate a high-resolution orthomosaic time series over a 5-month period of an Alpine glacier forefield characterized by a well-developed and heterogeneous stream ecosystem. We assess the performances of orthomosaic-derived visible band ratios and logistic models in mapping benthic biofilm distributions at high spatial and temporal resolutions. Aware that visible bands and ratios between them have limited capabilities in segmenting features based on their spectral response, we demonstrate that when basic mapping, but at high frequency, is necessary there is no need for expensive sensors.

2. Methods

2.1. Study site

The forefield of the Glacier d'Otemma is situated in Val de Bagnes (Valais, Switzerland) (Figure 1). The forefield has formed since the early 2000s in response to retreat of the Glacier d'Otemma, which has retreated at an average of 50 m per year (Mancini and Lane, 2020). The resultant fluvial braidplain is approximately 900 m long and 150 m wide and characterized by a well-developed floodplain drained by a complex and heterogeneous krial, krenal and rhithral stream system. The braidplain is active and continuously

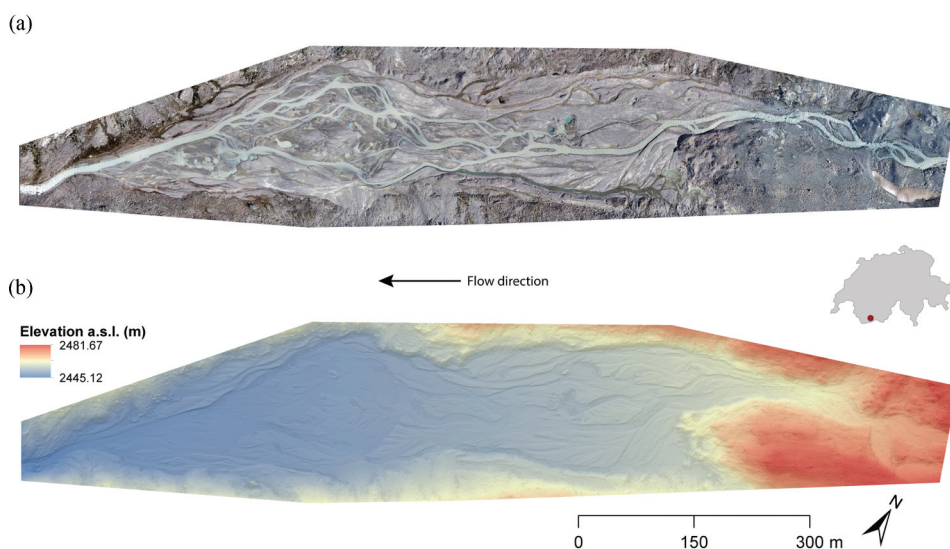


Figure 1. Forefield of the Glacier d'Otemma (Valais, Switzerland); Orthomosaic (a) and digital elevation model (b) of the study zone.

reworked during the melt-season (Mancini and Lane, 2020), typically constraining pioneer vegetation and benthic biofilms to the right-side terraces until rates of morphodynamic activity decline in the autumn.

2.2. Image and ground control point acquisition

RGB imagery was collected from late June to early September 2020 on 52 non-consecutive days with an additional acquisition date in November 2020. To collect the images, we deployed a DJI Phantom 4 Pro quadcopter, which is a well-established UAV platform in SfM-MVS photogrammetric studies (James et al., 2020). Relatively low-cost and low-weight, the quadcopter allows for pre-programmed flight missions due to its incorporated GPS. The integrated RGB camera has a 20 megapixel sensor, mechanical shutter, nominal 8.8 mm focal length, and stores images in both JPEG and RAW formats.

The forefield was imaged once or twice per day. Diurnal discharge variation related to the melt pattern of the glacier causes extensive inundation of the braidplain during the afternoon and evening. Therefore, we focused on the early morning flights (acquired from 06h30 onwards) for biofilm mapping. We used the freeware Pix4Dcapture (v. 4.8.0) to manage flight missions and geometries, and automatically collect images in JPEG format. Flight geometries were designed to produce high-precision datasets free of systematic error DEMs (following James et al. 2020) for further analyses of the forefield. Each set of flights was composed of: i) four grids with the camera looking at nadir (90°), image overlap set at 80% and a flight elevation of 80 m; and ii) 7 circular missions with the camera taking off-nadir and centre-looking pictures every 6° of the circles and flight elevation of 60 m. To ensure continuous mapping, singular grids intersected with each other. Each flight session took roughly 3.5 hours to complete and was composed of about 2'000 JPEG images. Geometries, flight path dimensions, and camera positions are shown in [Figure 2a](#).

In SfM-MVS photogrammetry, at least three well-scattered Ground Control Points (GCPs) are needed to scale, rotate and orientate DEMs and orthomosaics to a real-world coordinate system (Fonstad et al., 2013; Woodget et al., 2015). However, research has shown that GCPs are needed to improve the solution of the collinearity equations and to reduce the occurrence of systematic deformations in DEMs. The number of points needed is dependent on the spatial extent of the study site (James and Robson, 2014; James et al., 2017, 2020). We fixed 77 GCPs across the zone of interest ([Figure 2b](#)). We measured the GCPs at the beginning and end of the season with a differential GPS (dGPS) Trimble R10, and collected their absolute coordinates in the Swiss coordinate system CH1903+ to a precision of better than ± 0.01 m in the horizontal and ± 0.02 m in the vertical. The dGPS base station was located at the end of the floodplain and on the top of a bedrock hill to maximize the radio communication between the base and the rover. The base was corrected into the CH1903+ coordinate system using the fixed monitoring Swiss Federal Office for Topography provided via SwiPOS®.

2.3. Image processing and orthomosaic generation

The SfM-MVS photogrammetric processing was undertaken with Agisoft Metashape (v. 1.5.5) run on a dedicated workstation equipped with an AMD Ryzen 12-core processor (3.80 Ghz), 64 Gb RAM, and a GeForce RTX 2080 (8 Gb) graphic card allowing for GPU

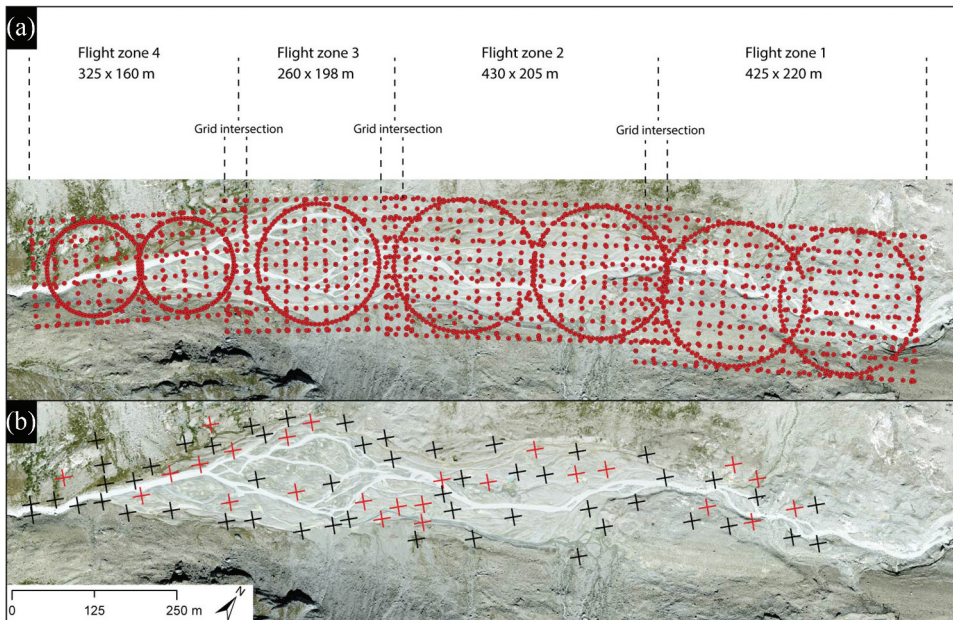


Figure 2. A) Flight geometries, camera positions and flight path dimensions. Image acquisition started at Flight zone 1, and take-off points were kept the same or similar throughout the season. b) Ground control point locations. Black GCPs were used in processing, while red GCPs were discarded after the Monte Carlo analysis. Orthomosaic ©swisstopo.

acceleration. To ensure strong (i.e. free of systematic deformations), reliable and replicable SfM-MVS photogrammetric processing within the totality of the datasets we followed the framework of James et al. (2017; 2020). Initially, we aligned the images of the first dataset (26 June 2020) to generate a sparse point cloud. We then explored how the different camera internal parameters (e.g. focal length, four radial and tangential distortion coefficients, principal point offsets, etc.) in the bundle adjustment influenced the 3D re-shaping of the sparse point cloud. To do so, we first used a Monte Carlo framework (James et al., 2017) in which different sets of camera internal parameters, so-called camera models (Table 1), were evaluated within the bundle adjustments by using a variable selection (but always 50%) of GCPs and 11 prescribed GCP accuracies (Table 1). Specifically, for each camera model investigated, we ran 1100 bundle adjustments, corresponding to 100 adjustments with 100 GCP combinations for each prescribed GCP accuracy.

Based on the results of the Monte Carlo simulations, model 3, which includes focal length, principal point offset (C_x, C_y), affinity and orthogonality parameters (B_1, B_2), radial (K_1, K_2, K_3) and decentering (P_1, P_2) distortions, delivered point clouds with the lowest probability of producing systematic errors even with the highest prescribed GCP accuracies. Second, for each camera model (Table 1) and by using the whole GCP population, we reconstructed (namely tie) point covariance maps (James et al., 2020) to detect visually systematic deformations in the point clouds. These maps showed the agreement between the tie point positions, and we found that model 3 delivered point clouds without any spatial structure related to the presence of systematic deformation.

Table 1. Summary of the parameters used within the Monte Carlo framework. We evaluated eight camera models found in classic SfM-MVS papers (James et al., 2017, 2020), where: f is the focal length, K_n is a radial distortion parameter, P_n is a decentring distortion parameter, C_x and C_y are principal point offset, B_n is an affinity and orthogonality parameter. The prescribed GCP accuracies (m) were chosen to cover a wide range of accuracies, from centimetres to metres, and refer to accuracies we may expect for each GCP.

Camera internal parameters (i.e. camera models)	Reference
Model 1: f, K_1	(James et al., 2020)
Model 2: f, K_1, P_2	(James et al., 2020)
Model 3: $f, C_x, C_y, B_1, B_2, K_1, K_2, K_3, P_1, P_2$	(James et al., 2020)
Model 4: $f, C_x, C_y, B_1, B_2, K_1, K_2, K_3, P_1$	(James et al., 2020)
Model 5: $f, C_x, C_y, K_1, K_2, K_3$	(James et al., 2017)
Model 6: $f, C_x, C_y, K_1, K_2, K_3, P_1, P_2$	(James et al., 2017)
Model 7: $f, C_x, C_y, B_1, B_2, K_1, K_2, K_3, K_4, P_1, P_2$	(James et al., 2017)
Model 8: f	(James et al., 2017)
Prescribed GCP accuracies (m) tested within the bundle adjustments	
0.001, 0.002, 0.005, 0.01, 0.02, 0.05, 0.10, 0.20, 0.50, 1.00, 2.00	
Percentage of GCPs used within the bundle adjustments	
10, 20, 30, 40, 50, 60, 70, 80, 90	

We then assessed the quality of the GCPs by using model 3 in 900 bundle adjustments, but varying the percentage of GCPs (Table 1) used in each bundle adjustment (James et al., 2017). Based on the Monte Carlo results, the RMSE of the XYZ components stabilized at 0.02 m corresponding to the use of 60% of the GCP ($n = 46$) into the bundle adjustment. However, the best 46 GCPs were not spatially well distributed, hence why we retained 52 GCPs (68%) and discarded the 25 GCPs showing the highest vertical/horizontal errors (Figure 2b).

The chosen camera model and GCPs were applied in the processing of the remaining datasets ($n = 53$). In addition to this, each sparse point cloud was inspected before the bundle adjustment: i) to remove tie points seen by two images only, ii) to remove poorly positioned tie points (e.g. beneath the reconstructed surface), and iii) to remove images having fewer than 1000 projections in the tie points and error greater than 1 pixel (following James et al., 2020). With our workstation configuration and step-wise procedure, it took roughly 8 h per dataset to produce results with minimal 3D and optical distortions, fully georeferenced DEMs at 20 cm, and orthomosaics at 5 cm spatial resolutions.

2.4. Orthomosaic normalization

Multi-temporal images are often difficult to compare due to non-scene dependent changes, such as in sensor or illumination conditions (Schott et al., 1988; Du et al., 2002; Song and Woodcock, 2003; Liu et al., 2007; Bao et al., 2012). In our case, the sensor was the same throughout the field season (i.e. DJI Phantom 4 Pro's camera), but illumination changed during image acquisition because of differences in cloud coverage or sun position (both within the same dataset and between datasets).

The easiest way to deal with this problem is to have a dataset-specific image calibration based on individual scenes. Ideally, it would be possible to use one or a subset of scenes to produce a general classification rule that could be applied to all scenes. This requires that each orthomosaic must have similar signatures, in our case requiring that pixels composing

non-biotic features (e.g. rocks, sand) should reflect the same quantity (i.e. digital numbers) of red, green, and blue bands throughout the measurement period. This is particularly important when a common logistic model (i.e. reference) is applied to a visible band ratio. To achieve this, we tested scene-to-scene normalization (Schroeder et al., 2006) using a relative radiometric normalization, the Pseudo-Invariant-Feature (PIF) method. This method aims to correct each image to a reference by applying a linear model on pixels that should not have experienced any reflectivity change between the two acquisitions (Schott, et al., 1988; Du et al., 2002; Bao et al., 2012). Typically, PIFs are artificial objects (e.g. roofs, roads, etc.) that do not show seasonal or biological activity with almost constant reflectivity through time (Schott et al., 1988).

In our study area, there was a lack of artificial objects, and the only ones suitable for a traditional PIF normalization were the GCPs scattered on the floodplain, which were black and yellow and large enough to allow for single pixel picking. We visually inspected the set of orthomosaics, and we selected 45 single pixels within the eight clearest GCPs. Furthermore, we sampled an additional 37 single pixels of pure and constant-through-time dry sand and/or sediment to complete the PIF population ($n = 82$). After several attempts, we found that 82 PIFs provided a good trade-off between normalization quality and processing time. We also decided to use single pixels instead of averaging groups because of the important sub-decimetre variation in pixel colours. To cope with changes in light conditions and sun position, through the summer, we divided the dataset into three sub-datasets: i) Group 1, consisting of 19 datasets spanning from 26 June to 19 July 2020, using 14 July as a reference; ii) Group 2, consisting of 22 datasets spanning from 21 July to 21 August 2020, using 26 July as a reference; and iii) Group 3, consisting of 11 datasets spanning from 23 August to 13 September 2020, using 14 July as a reference. Group 3 shared the same reference as Group 1, although it is temporally distant because we noted that 14 July had good normalization performances on the images of the third group. The orthomosaic of 5 November 2020 was treated separately and called Group 4, and due to snow coverage, no correction was applied.

Within each group and on a band-by-band basis, we regressed linearly the digital numbers of the reference PIFs against the digital numbers of the PIFs of each orthomosaic to be normalized. We then applied the three linear models to the totality of the pixels composing the single-band (red, green, and blue) orthomosaics to ultimately obtain radiometric normalized bands. We assessed the quality of the normalizations by evaluating the root mean square error (RMSE) of pixel digital numbers before the normalization and after as compared with the relevant reference image, as well as by visually inspecting how the histograms changed after applying the linear models.

The orthomosaic normalization was performed through a Matlab (R2018a) routine. Even though PIF normalization should allow transferability of calibration models for biofilm mapping, we decided to also compare results with i) the non-normalized but group sorted orthomosaics and ii) a scene-by-scene calibration model.

2.5. Visible band ratios, logistic models, and probability maps

The non-normalized individual scenes and the normalized bands were used to compute visible band ratios, which have the advantage of summarizing the information of the three visible bands into one. Such ratios have been widely used in vegetation detection or

crop studies since the 1970s (e.g. Tucker, 1979; Woebbecke et al., 1995; Kawashima and Nakatani, 1998; Meyer et al., 1998; Adamsen et al., 1999; Louhaichi et al., 2001; Gitelson et al., 2002; Meyer and Neto, 2008; Saberioon et al., 2014), but also in aquatic studies (Xu et al., 2018). Here, we computed eight band ratios (Table 2) and tested their performance in mapping biofilms.

To classify the orthomosaics into biofilm distributions across the whole floodplain, we first developed training/calibration and validation datasets for each orthomosaic. These datasets were based upon the selection of 150 sites at the single pixel level that were biofilms and covering the range principal colour assemblages present on the floodplain (i.e. red-brown and green). The site selection was straightforward because “glacial” biofilms have a distinctive colour compared to the dry or wet un-colonized substrata (e.g. grey), and this was clearly distinguishable on the orthomosaics at the spatial resolutions we were using. An additional 150 sites were selected across the floodplain to account for the un-colonized substrata. This was the calibration dataset. We then selected another set of sites ($n = 300$, 50% biofilm), using the same criteria but with no overlap with the calibration dataset. The biofilm mapping was then based upon training logistical models using the calibration dataset.

The outcome of the logistic model was a probability of biofilm being present. For validation, we converted the probability (0 to 1) into binary values (0 or 1) by assigning 0 (not biofilm) to sites with probability <0.5 and 1 (biofilm) to sites with probability >0.5 . These predictions were combined with the validation to provide confusion matrices (i.e. true positive/negative vs. false positive/negative) and hence to assess model performance by comparing prediction accuracies, precisions, recalls, F-scores, and Matthews Correlation Coefficients (MCC) (Chicco and Jurman 2020).

The logistic models were applied in two ways. First, to understand the optimal choice of logistic regression model type (Table 2) we applied each type to the reference images (14 July for Groups 1/3 and 20 July for Group 2) and the November image (Group 4). Second, having identified an ideal model type, we trained a scene-by-scene model for each date to be our reference probability map dataset. This made use of calibration data and validation data particular to each scene. This approach is labour-intensive, but it avoids the need to make assumptions about the temporal stability of the logistical models derived, and no normalization is required. We call these the reference datasets. Finally, we applied the calibrated logistic models selected for the two reference images to both the raw and the normalized orthomosaics according to the group each

Table 2. Band ratios tested for benthic biofilm. R, G, and B are non-normalized digital numbers (i.e. R, G, and B ranging from 0 to 255); r, g, b are normalized digital numbers (i.e. R, G, and B ranging from 0 to 1).

Name	Acronym	Formula	Source
Chromatic Coordinates of Red	RCC	$R/(R+G+B)$	Woebbecke et al. (1995)
Normalized Green-Red Difference Index	NGRD	$(g-r)/(g+r)$	Tucker (1979)
Excess Red Vegetation Index	ExR	$1.4*r-g$	Mao et al. (2003)
Excess Green Vegetation Index	ExG	$2*g-r-b$	Woebbecke et al. (1995)
Green Leaf Index	GLI	$((G-R)+(G-B))/(G+R+G+B)$	Louhaichi et al. (2001)
Visible Atmospherically Resistant Index	VARI	$(G-R)/(G+R-B)$	Gitelson et al. (2002)
Kawashima and Nakatani Index	KANA	$(R-B)/(R+B)$	Kawashima and Nakatani (1998)
Red Green Ratio Index	RGRI	R/G	Saberioon et al. (2014)

orthomosaic was in. Moving to calibration based upon a small number of references significantly reduces workloads, but makes the analysis more dependent on the reliability of normalization.

We produced three first probability map datasets: i) single – with a different calibration model for each scene, the single datasets; ii) raw – using the Group 1/3 and Group 2 reference calibration models and applied to non-normalized imagery; and iii) normalized – as per (ii) but using normalized imagery. All logistic regressions, validations, statistics and probability maps were performed in Matlab (R2018a).

2.6. Micro-topography shadow modelling

The effect of the floodplain micro-topography on shading and hence on the probability map quality was also investigated. We avoided exploring the shadowing effect of the surrounding peaks because, when present, it only affected the very upstream part of the study zone. We also did not develop a physically based treatment of the shadowing effect caused by clouds because of a lack of cloud cover data to include in a model. The micro-topography shadowing effect was, to varying degrees, always present and it was caused either by large boulders or by steep river banks. Normalization could not correct for this.

We modelled the micro-topography shadow by applying to our DEMs a potential solar radiation model (Kumar et al., 1997). The model accounts for the acquisition time and date (in our case the start and end of each UAV survey), the local topography using our DEMs, and latitude of the study zone, and it models the potential solar radiation in W/m^2 received during the selected period. Shadows were easily identified due to their low solar radiation, and subsequently masked binarily to exclude those pixels from being mapped in our probability maps. A new set of probabilistic maps was generated from the previous three datasets, and they are called single-shadow, raw-shadow, and normalized-shadow.

2.7. Occupation maps and noise assessment

Each scene produced a map showing the probability of biofilm occurrence. To understand how biofilms develop through time, we calculated the cumulative presence (in days) of biofilm in each pixel of the study zone, which we call an occupation map. In doing so, we excluded the probability map of November because of the significant time since the last summer acquisition date (September 13). To produce the occupation maps, we firstly converted the pixel probability in binary classification by assigning 0 to pixels with probability <0.5 and 1 to pixels with probability >0.5 . We then multiplied each binary map by a scalar representing the time-lag between two given acquisition dates (i.e. time-lag: $[t_{n+1} - t_{n-1}]/2$), and finally summed up the results to obtain the occupation (0–80 days) that biofilm was present in each pixel. Occupation calculations were performed in Matlab (R2018a), but maps were then exported in .ascii-format and converted into a suitable format (.tiff) for ArcMap (v. 10.5.1). In the GIS environment, we masked the study zone to exclude the vegetated edges, the sparse pioneer species across the floodplain, and the GCPs.

These occupation maps are of significance for understanding biofilms because the duration of occupation likely influences the duration and intensity of ecosystem engineering that the biofilm can perform. Thus, to understand how sensitive occupation maps are to normalization and shadow correction, we take the single scene accumulation map without shadow correction as a reference. We then compare the generated maps: i) using the single scenes, shadow corrected; ii) the reference models applied to the raw scenes, shadow uncorrected and corrected; and iii) the reference models applied to the normalized scenes, shadow uncorrected and corrected to this reference. We call these comparisons Occupations of Difference (OoD).

We also attempted to calculate noise in the occupation maps. First, in this kind of environment, biofilms may form rapidly, over the order of days, but also be destroyed rapidly such as by a lateral shift in the river channel. This would produce a run of time periods where biofilm are present followed by, if destroyed, a run of time periods where biofilms are absent until conditions again allow biofilm development. Noise would then interrupt these runs until, in the ultimate extreme, the biofilm present-absent time series is completely random. To assess this, we undertook a run test to lower the probability, for each pixel, that an occupation map is based upon non-randomly distributed presence-absence through time. The lower the p -value the less a pixel is affected by noise and the more likely that the occupation is reflecting true biofilm growth and destruction. We call this the occupancy noise map and we calculated it for single, raw, and normalized datasets with and without shadow.

We then created a new set of occupation maps in which we used the occupancy noise maps to exclude occupation pixels that had less than 95% ($p < 0.05$) probability of reflecting true biofilm dynamics in a given dataset.

3. Results

3.1. Identification of logistic regression model type

3.1.1. Groups 1 and 3

The band ratios derived from the orthomosaic for 14 July 2020 were used to train 8 logistic models. The NGRD-, ExG-, GLI-, VARI-, and RGRI-derived models struggled to find a substantial separation between pixels with or without biofilms (see supplementary information). The ExR-derived model behaved slightly better compared to the previous ones, whilst the RCC-, and KANA-derived models were able to find a more consistent spectral separation (see supplementary information).

Table 3 shows the validation results based upon sites not used to train these previous models. Not surprisingly, models with a poor separation between biotic and abiotic pixel values during training underperformed (e.g. ExG and GLI, Table 3). To differing degrees, RCC, NGRD, ExR, VARI, and RGRI performed well when validated, but KANA produced the best validation results and was therefore selected as the model to map biofilm distributions for groups 1 and 3.

3.1.2. Group 2

The eight models trained for 26 July did not significantly differ from the models of groups 1 and 3 (see supplementary information). Findings between groups are consistent: NGRD-, ExG-, GLI-, VARI-, and RGRI-derived models were again not able to substantially separate

Table 3. Logistic regression coefficients and performances of the selected index-derived binary classifications for groups 1 and 3.

	β_0	β_1	Accuracy	Precision	Recall	F1	MCC
RCC	-129.13	361.94	0.98	0.99	0.97	0.98	0.97
NGRD	-4.36	-168.65	0.89	0.93	0.84	0.88	0.85
ExR	-35.83	221.51	0.94	0.96	0.91	0.94	0.92
ExG	-0.30	35.64	0.69	0.70	0.68	0.69	0.47
GLI	-0.30	47.87	0.69	0.70	0.68	0.69	0.47
VARI	-4.05	-88.96	0.86	0.91	0.80	0.85	0.80
KANA	-8.12	107.63	0.98	0.99	0.97	0.98	0.98
RGRI	-84.34	80.06	0.89	0.93	0.84	0.88	0.85

Table 4. Logistic regression coefficients and performances of the selected index-derived binary classifications for group 2.

	β_0	β_1	Accuracy	Precision	Recall	F1	MCC
RCC	-528.58	1447.96	0.99	0.97	1.00	0.99	0.97
NGRD	-3.38	-99.10	0.95	0.91	0.99	0.95	0.91
ExR	-28.27	163.54	0.98	0.97	1.00	0.98	0.97
ExG	-2.04	87.34	0.86	0.94	0.77	0.85	0.81
GLI	-2.06	118.35	0.86	0.94	0.77	0.85	0.81
VARI	-2.88	-53.27	0.91	0.86	0.99	0.92	0.84
KANA	-27.84	280.36	0.99	0.97	1.00	0.99	0.97
RGRI	-49.29	46.01	0.96	0.93	0.99	0.96	0.92

biotic and abiotic pixels. The ExR-derived model was slightly better, but the RCC- and KANA-derived models were the best at finding the natural boundaries between abiotic and biotic pixels (see supplementary information).

As expected, the validation (Table 4) results for 26 July followed those for 14 July. The ExG- and GLI-derived models underperformed compared to the others, while the NGRD, VARI, and RGRI models were overall acceptable. The ExR-derived model was excellent, but still slightly worse than the RCC- and KANA-derived models. The RCC- and KANA-derived models showed equal performances, but we selected the KANA model to be consistent with groups 1 and 3.

3.1.3. Group 4

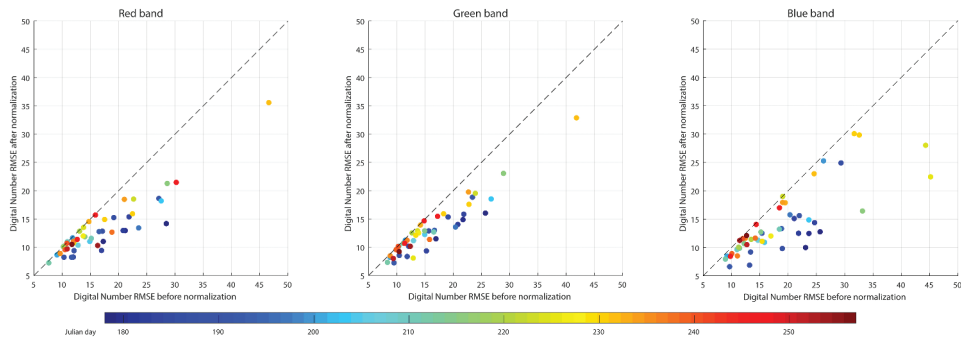
Overall, the models for the November mosaic behaved in a similar way to the July datasets, with the NGRD-, ExG-, GLI-, VARI-, and RGRI-derived models still being unable to find a substantial boundary between abiotic and biotic pixels. ExR-, RCC-, and KANA-derived models found more obvious separations (see supplementary information).

Validation results (Table 5) did not differ significantly from July results, with ExG- and GLI-derived models having the lowest performances within the band ratios. NGRD-, VARI-, and RGRI-derived models performed slightly better in comparison with the July datasets, while the KANA-derived model performed slightly worse. In this case, the RCC models had a better performance compared to the KANA model, but the difference was small (1% in recall); therefore, we kept the KANA-derived model as with the previous groups such that our methodology is consistent.

Based on these results, the KANA-derived model was selected as the type of logistical regression for the subsequent analyses.

Table 5. Performances of the selected index-derived binary classifications for group 4.

	β_0	β_1	Accuracy	Precision	Recall	F1	MCC
RCC	-61.54	171.01	0.98	0.99	0.98	0.98	0.98
NGRD	-1.85	-96.32	0.98	0.99	0.97	0.98	0.97
ExR	-18.76	120.81	0.98	0.99	0.97	0.98	0.97
ExG	-2.25	39.01	0.74	0.73	0.77	0.75	0.55
GLI	-2.28	53.68	0.74	0.73	0.77	0.75	0.55
VARI	-1.79	-58.11	0.98	0.99	0.97	0.98	0.97
KANA	-6.48	60.42	0.98	0.99	0.97	0.98	0.98
RGRI	-46.01	44.21	0.98	0.99	0.97	0.98	0.97

**Figure 3.** Digital Numbers (DNs) related RMSE of the pixels composing the non-reference images before and after normalization in comparison with their relevant reference orthomosaics for the red band, the green band and the blue band. Dates are in Julian days.

3.2. Orthomosaic normalization

Figure 3 shows the digital number RMSE by band for each non-reference orthomosaic, both before and after normalization and in comparison with the relevant reference one (14 July for Group 1 and Group 3 datasets; 26 July for Group 2 datasets). The normalization behaved similarly between the bands.

Group 1 (26 June to 19 July or Julian day 178 to 201) showed a generalized important RMSE reduction, particularly on the red ($\bar{x}=-28.8\%$; $\sigma=12.9$) and blue ($\bar{x}=-32.5\%$; $\sigma=\pm 15.6$) bands as compared to the green one ($\bar{x}=-24\%$; $\sigma=\pm 10.2$). Group 2 (21 July to 21 August or Julian day 203 to 234) had a tendency towards improvement (red band: $\bar{x}=-13.2\%$; $\sigma=\pm 10.6$; green band: $\bar{x}=-13.6\%$; $\sigma=\pm 9.7$; blue band: $\bar{x}=-19.9\%$; $\sigma=\pm 14.5$), but RMSE reduction was variable within the orthomosaics. Dates closer to the group 2 to 3 transition profited from a RMSE reduction through the normalization, but RMSEs still remained high (especially within the blue band). Dates closer to the group 1 to 2 transition had lower RMSEs before the normalization, and only a limited improvement was observed afterwards. Group 3 (23 August to 13 September or Julian day 236 to 256) had RMSEs <20 DNs before normalization (except 3 August), and the normalization was not particularly effective and the RMSE reduction was generally small. We observed a RMSE reduction of 14.3% ($\sigma=\pm 12.5$) for the red band, of 9.3% ($\sigma=\pm 8.3$) for the green band and of 9.9% ($\sigma=\pm 8.3$) for the blue band.

The generalized RMSE reductions resulted from applying the specific band-by-band linear models to normalize the DNs of the non-reference orthomosaics such that they are closer to those of the reference ones. In some cases, however, the RMSEs did not decrease to low magnitudes or decreased differently between the bands, and this translated into poorly normalized orthomosaics. The orthomosaic of 19 August (Figure 4) is an example of a poor normalization. The PIF points of the red and green bands were highly dispersed (resulting in poor R^2) and most of them deviated towards the brighter side of the colour tone (i.e. left of the 1:1 line) before applying the models. As expected, their corresponding models sat on the brighter side of the colour tone (y-intercepts of >50 and slopes of roughly 0.8). The blue band was slightly better and the PIF points less dispersed ($R^2 = 0.9$). The blue model had better y-intercept and slope compared to the previous two bands, but tones with DNs >125 were translated into brighter tones whilst tones with DNs <125 into darker ones. The poor models then translated into a poorly normalized orthomosaic (Figure 4b), with an unnatural colour grading and very different as compared to the reference image. This is also visible from the histogram of the normalized orthomosaic (Figure 4b), with the blue band that lost some information while the red and green bands gained counts in the bright tail of the histogram. Overall, the orthomosaic was brighter and green tones were enhanced.

The 7 July orthomosaic (Figure 5) is, in contrast, an example of a good normalization. The band-related RMSE magnitudeness were low before the normalization (± 10 – 13 DNs) and the PIF points well-aligned. The linear models showed high R^2 , slopes of 0.9 and y-intercepts ranging from 19.21 to 24.29 (Figure 5a). Such slopes and y-intercepts enhanced the brightness of the bands, slightly attenuating the dark tones. As a response, the left tail of the histogram (i.e. the darker tones) of the normalized orthomosaic (Figure 5) was reduced, eventually resembling the master histogram.

An example of an excellent PIF normalization is shown for 30 July (Figure 6). Compared to the previous two orthomosaics, in this case the band RMSE magnitudes were already low (<9 DNs) before the normalization and the PIF points were well aligned. As a result, the linear models had very high R^2 , slopes close to 1 and y-intercepts close to 0 (Figure 6a). For these reasons, the application of such models should have provided the best normalization possible for this orthomosaic (Figure 6b), even though pre-normalization differences were already very low. A comprehensive summary of the normalization performances, including slopes and y-intercepts for each model, can be found in the supplementary information for this paper.

3.3. Quantitative evaluation of the PIF normalization

We compared the performances of the PIF normalization models (i.e. normalized) with the performances of the raw mosaics (Figure 7a). We also evaluated the normalized (Figure 7b) and raw (Figure 7c) mosaics in comparison to the single calibrations.

Overall, using the reference models (14 July 2026 July) on the raw and normalized mosaics for other dates produced good results (Figure 7a). Surprisingly, the raw datasets had a substantially better performance than the normalized ones. Performance deterioration was more severe in Group 2 as compared to the less divergent Groups 1 and 3. When

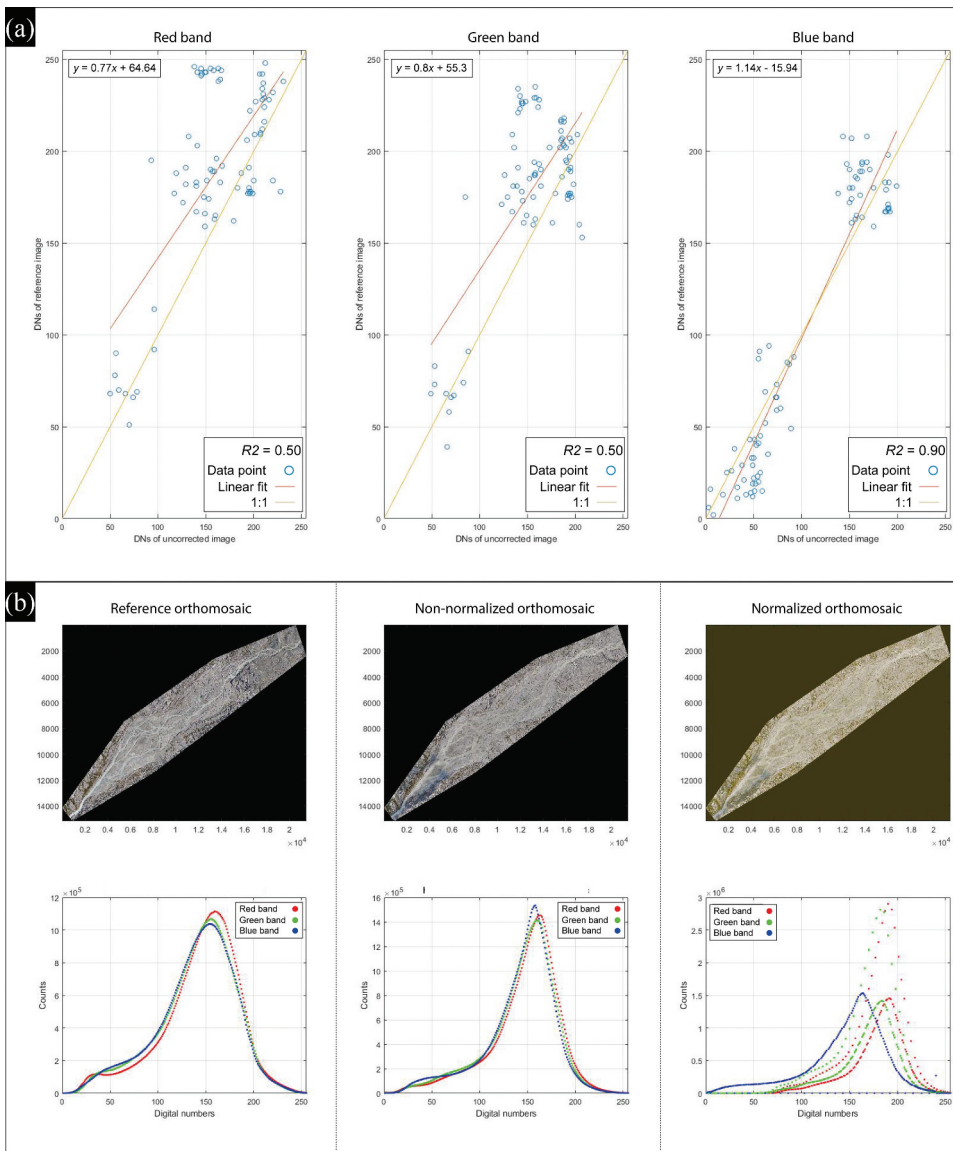


Figure 4. Example (19 August, Group 2) of a poor PIF normalization. a) Linear models and corresponding R^2 ; b) Comparison between reference image (26 July), non-normalized orthomosaic (non-reference) and normalized one.

compared to the single models, the normalized dataset (Figure 7b) had a clearly poorer performance, and this was accentuated in Group 1 and notably Group 2, reflecting the difficulties encountered during the PIF normalization. The raw datasets (Figure 7c) were more similar to the single models, and even better in some cases. Interestingly, Group 2 datasets produced better results, reflecting again that normalization could lead to model deterioration.

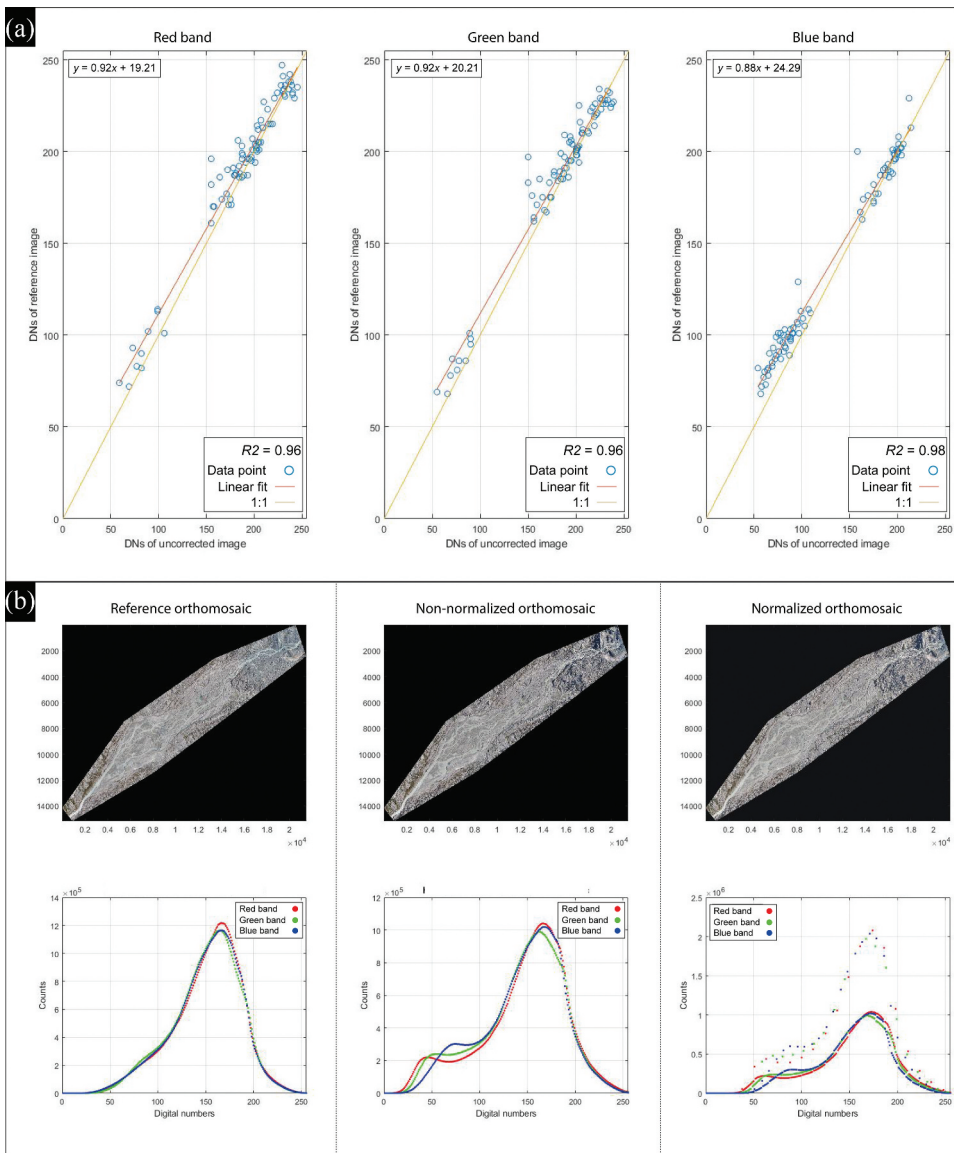


Figure 5. Example (7 July, Group 1) of a good PIF normalization. a) Linear models and corresponding R^2 ; b) Comparison between reference image (i.e. 14 July), non-normalized orthomosaic (non-reference) and normalized one.

3.4. Shadow model

An example of the micro-topography model and the subsequent biofilm presence/absence masking is presented in Figure 8. Moving water in glacial channels often created artefacts in the DEMs, and those in turn created micro-relief at the resolution we used, and hence shadows. Unlike true micro-topography shadows, such zones had a minimal effect on the shadow masks, since they were located on the surface of moving glacial water, i.e. where biofilms did not develop. Biofilm probability maps were binarized (Figure 8d)

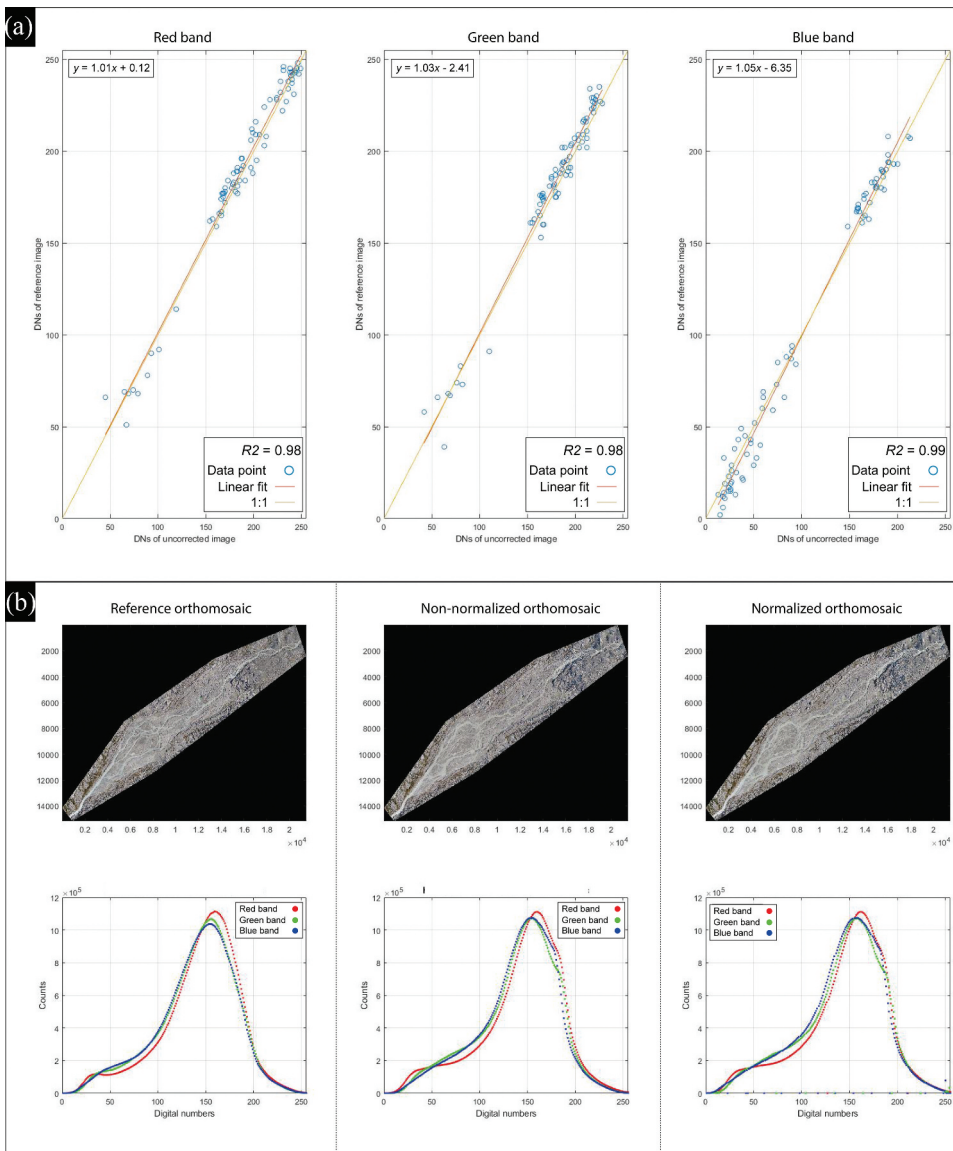


Figure 6. Example (30 July, Group 2) of an excellent PIF normalization. a) Linear models and corresponding R^2 ; b) Comparison between reference image (i.e. 26 July), non-normalized orthomosaic before correction and normalized one.

before being used as input in the occupation map calculations, but we also explored how biofilm presence/absence changed if micro-topography shadow areas were excluded from being mapped (Figure 8e). True micro-topography shadows were typically restricted to banks and boulders (Figure 8c). Removing micro-topography caused shadows did indeed remove zones mapped as biofilms. However, there were also some examples of micro-relief where biofilms were present in zones of shadow, notably around small boulders.

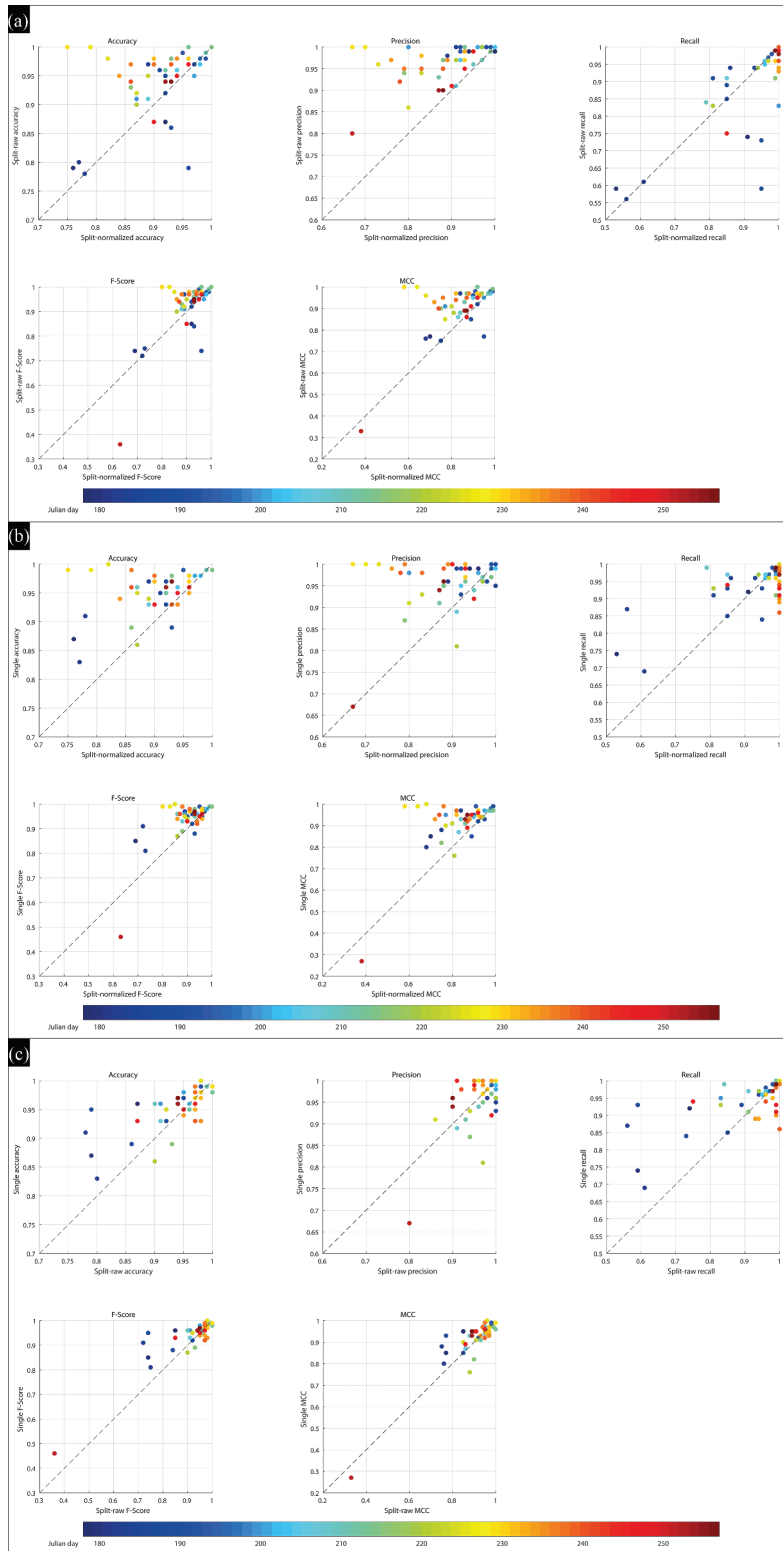


Figure 7. A) Comparison between normalized and raw performances, b) normalized and single performances, and c) raw and single performances.

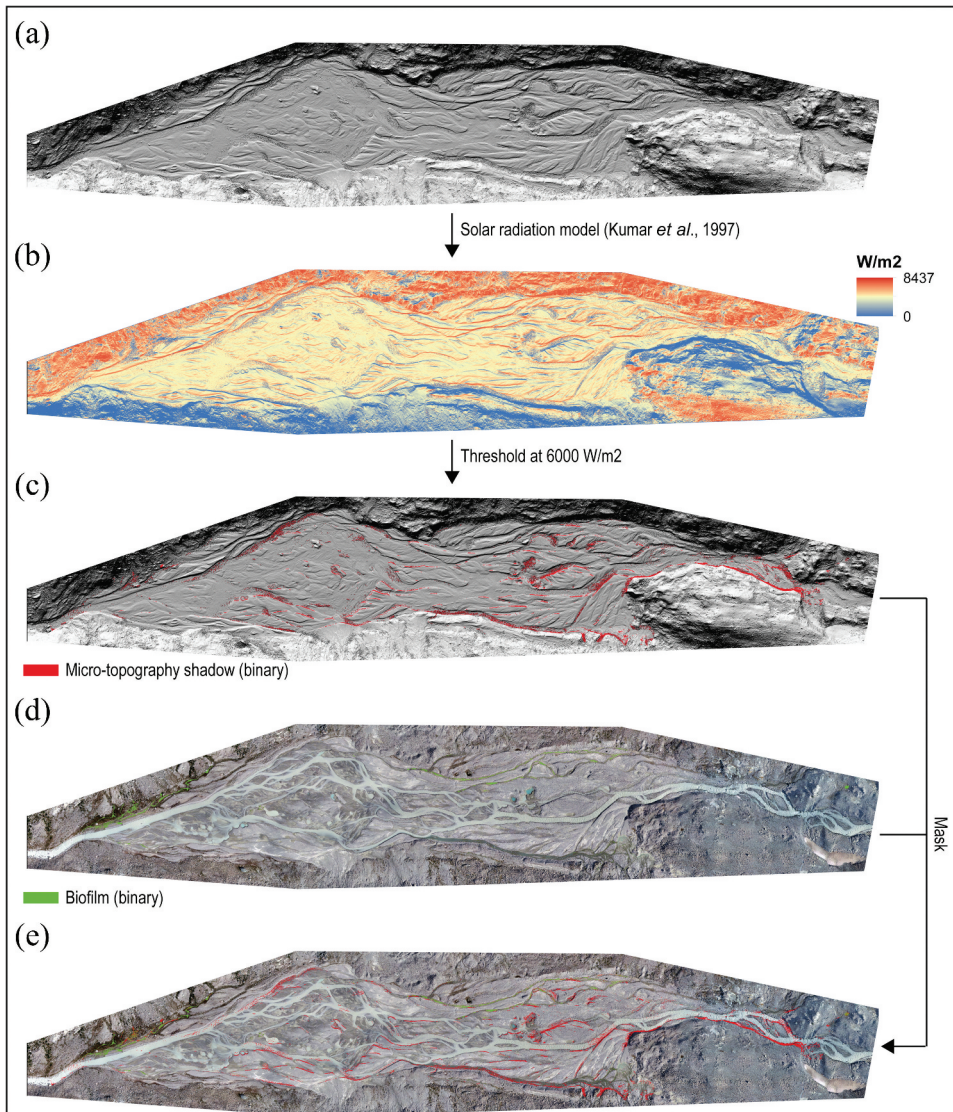


Figure 8. Example of the applied micro-topography shadow model to a binary presence/absence biofilm map from 14 July: a) Hillshaded DEM, b) modelled solar radiation, c) micro-topography shadow, binarized at 6000 W/m^2 , d) presence/absence of biofilm (input of the occupation map), and e) presence/absence of biofilm masked by micro-topography shadows. Binarized micro-topography model and biofilm presence/absence were masked to exclude the edges.

3.5. Evaluation of the resultant biofilm maps

Occupation maps for the single, raw and normalized, with and without accounting for micro-topography shadow, are shown in Figure 9. Qualitatively, results tend to agree among themselves, with the highest cumulative presence of biofilms in channels located on the edges of the topographic right-side of the braidplain.

The use of the single and single-shadow probability datasets (Figure 9a,b) produced clusters of biofilm occupation that were very similar to each other, and only marginal differences were visible, most of which were located on the transitions between steep banks that created micro-topography shadows and water surfaces. Single pixels with an occupation range of 1 to 10 were present but widely distributed, found especially in the centre-part of the floodplain, and were likely to be noisy. Results of the raw and raw-shadow derived occupations maps (Figure 9c,d) did not significantly differ from the single and single-shadow ones, although in both scenarios there were fewer pixels within the 1 to 10 day range in the centre-part of the braidplain. Similarly to the single datasets, micro-topography shadow removal did not substantially modify clusters of biofilm occupation. When occupation was calculated with the normalized datasets (with and without shadows; Figure 9e,f), significant biofilm presence over periods of 1–10 days was detected even in the active braidplain. This was not the case for the single datasets (Figure 9a,b) and the raw ones (Figure 9c,d), suggesting the presence of systematic mapping errors (i.e. spectral confusion plus noise) in the normalized probability maps.

Comparison between single and single-shadow Occupation of Difference (OoD) maps (Figure 10a) showed that the single-shadow map gave slightly lower occupation (mean difference: -0.008 days) as compared to the single map, and some noise was successfully removed from the upstream half of the floodplain. However, the right-side channels of the single-shadow occupation map showed anomalously lower reduced occupation (mostly within the -5 day range) that resulted from the exclusion of pixels affected by micro-topography shadow, though those pixels were actually biofilm. Comparison between the raw occupation and single occupation maps with no shadow correction (Figure 10b) showed more heterogeneous differences, although the mean difference was still negative (-0.01). The centre-part of the braidplain had less noise, but there was either under- or over-estimation of occupation days in the side channels, both on the left and right sides of the braidplain. This result suggested that when applied to different dates the reference models (i.e. 14 July for groups 1 and 3, and 26 July for Group 2) were either too weak, creating over-estimation, or too strong, creating under-estimation. The OoD maps with the raw-shadow dataset (Figure 10c) were similar to that of the raw dataset (Figure 10b), but the mean difference was slightly higher, suggesting that micro-topography shadow masking had a stronger impact. Not surprisingly, the normalized occupation-related OoDs (Figure 10d,e) showed systematic overestimation across the whole floodplain suggesting that the reference models were typically too weak such that many non-biofilm pixels (e.g. wet sediments) were mapped as being biofilms due to pixel values greater than the 0.5 selected threshold.

3.6. Occupancy noise maps and p -value corrected occupation maps

The probability maps show those zones where the time-series of occupancy/non-occupancy is systematic ($p < 0.05$) and random ($p > 0.05$), the latter indicating possible noise (Figure 11). The single (Figure 11a,b) and raw (Figure 11c,d) scenarios showed similar results: i) single pixels (or small clusters) in the centre-part of the floodplain that may have a high total occupancy, but this occupancy is random and so likely to be noisy,

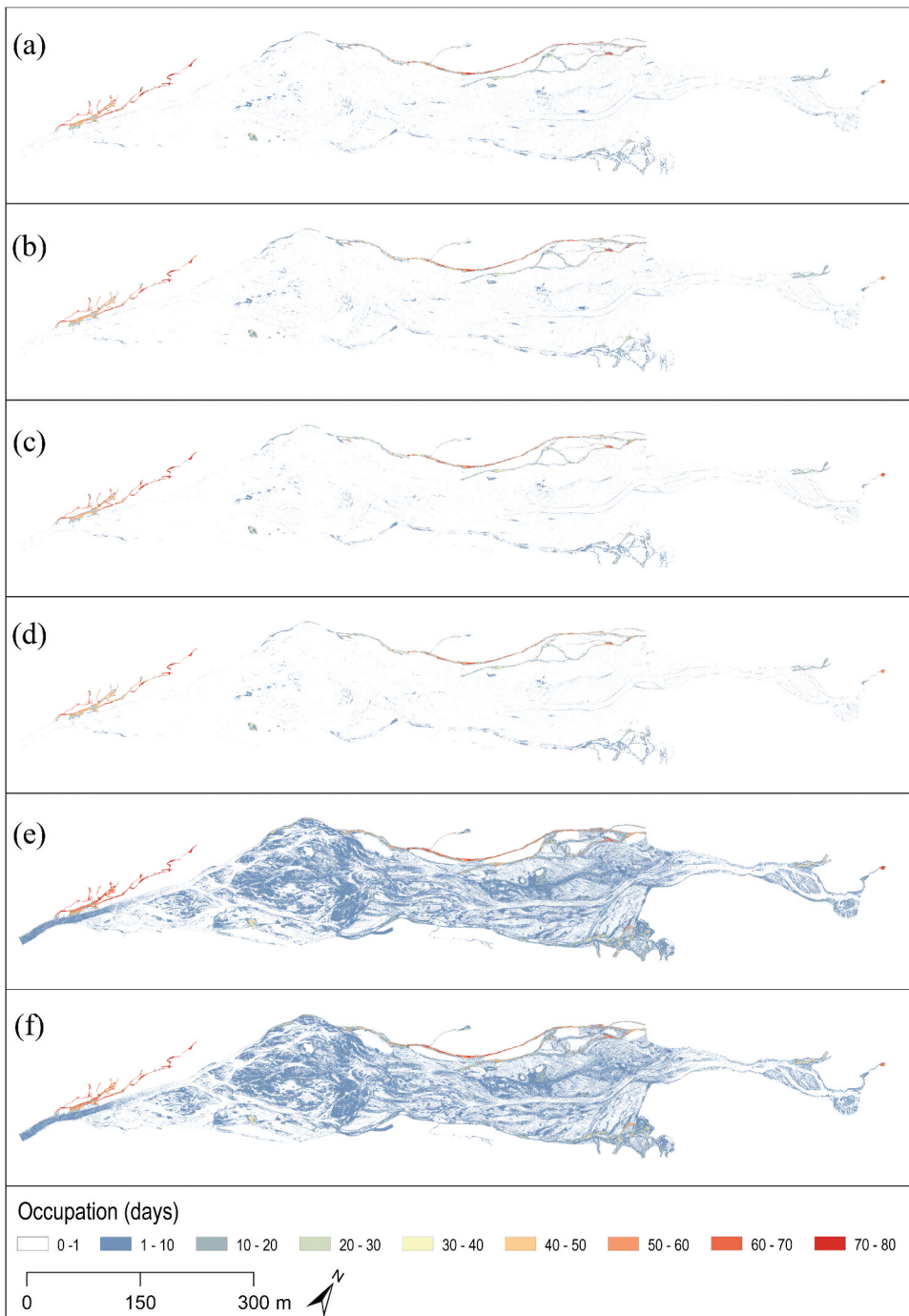


Figure 9. Occupation (in days) of biofilms on the floodplain of the Glacier d'Otemma during the period 26 June to 13 September 2020. Occupation calculated from a) the single dataset, b) the single-shadow dataset, c) the raw dataset, d) the raw-shadow dataset, e) the normalized dataset, and f) the normalized-shadow dataset.

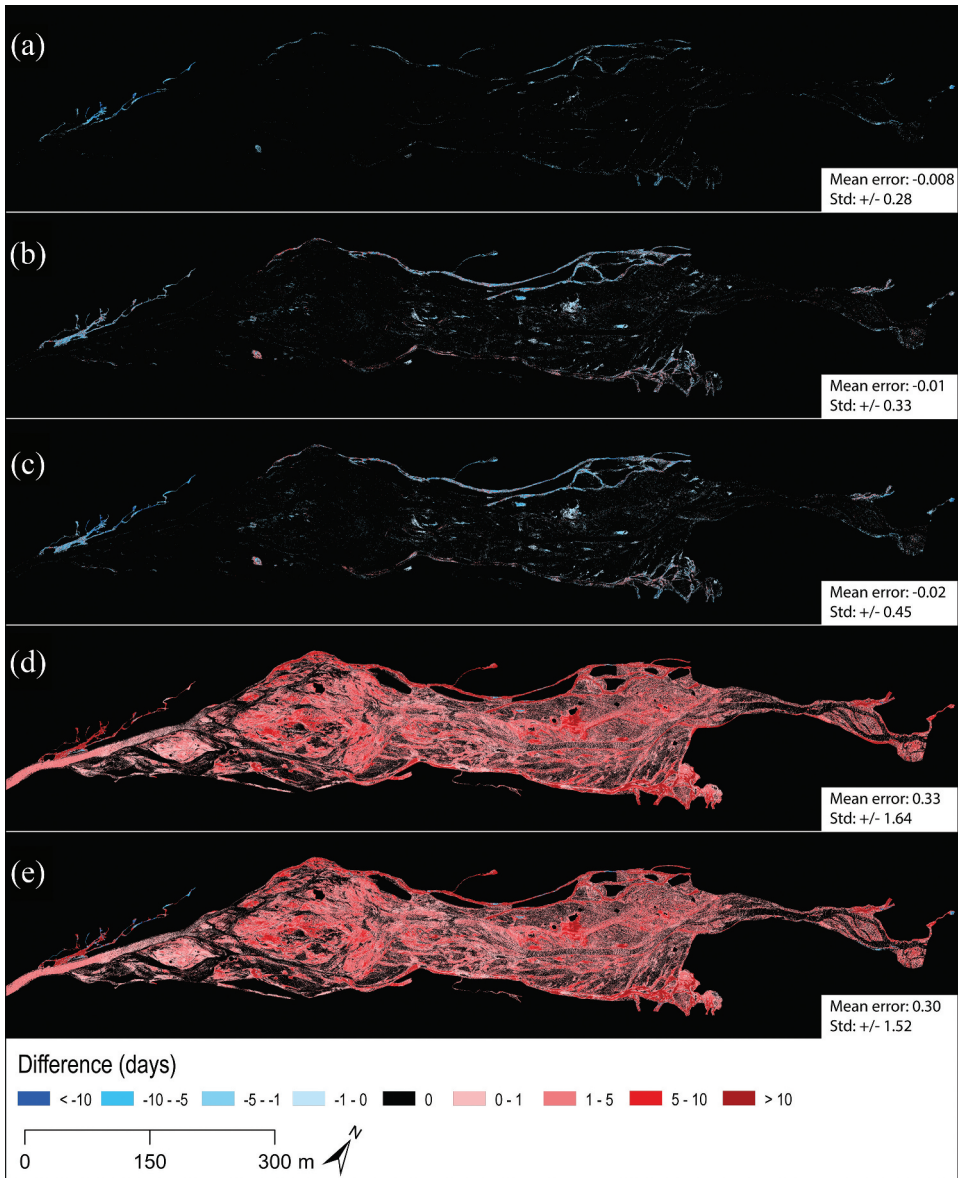


Figure 10. Occupations of Difference (OoD): a) Single-shadow minus single, b) raw minus single, c) raw-shadow minus single, d) normalized minus single, and e) normalized-shadow minus single.

and ii) zones in the side channels that also appeared to have some random occupancy. The normalized scenarios (Figure 11e,f) confirmed results in Section 3.5, with biofilm occupancy in the active braidplain being random and over-estimated.

We then used the occupancy noise maps to exclude pixels with $p > 0.05$ from being considered biofilm pixels in the occupation map calculations. A new set of occupation maps was generated (Figure 12). Most of the salt and pepper noise was successfully removed from the single and raw scenarios (Figure 12(a-d)) using this criterion. The

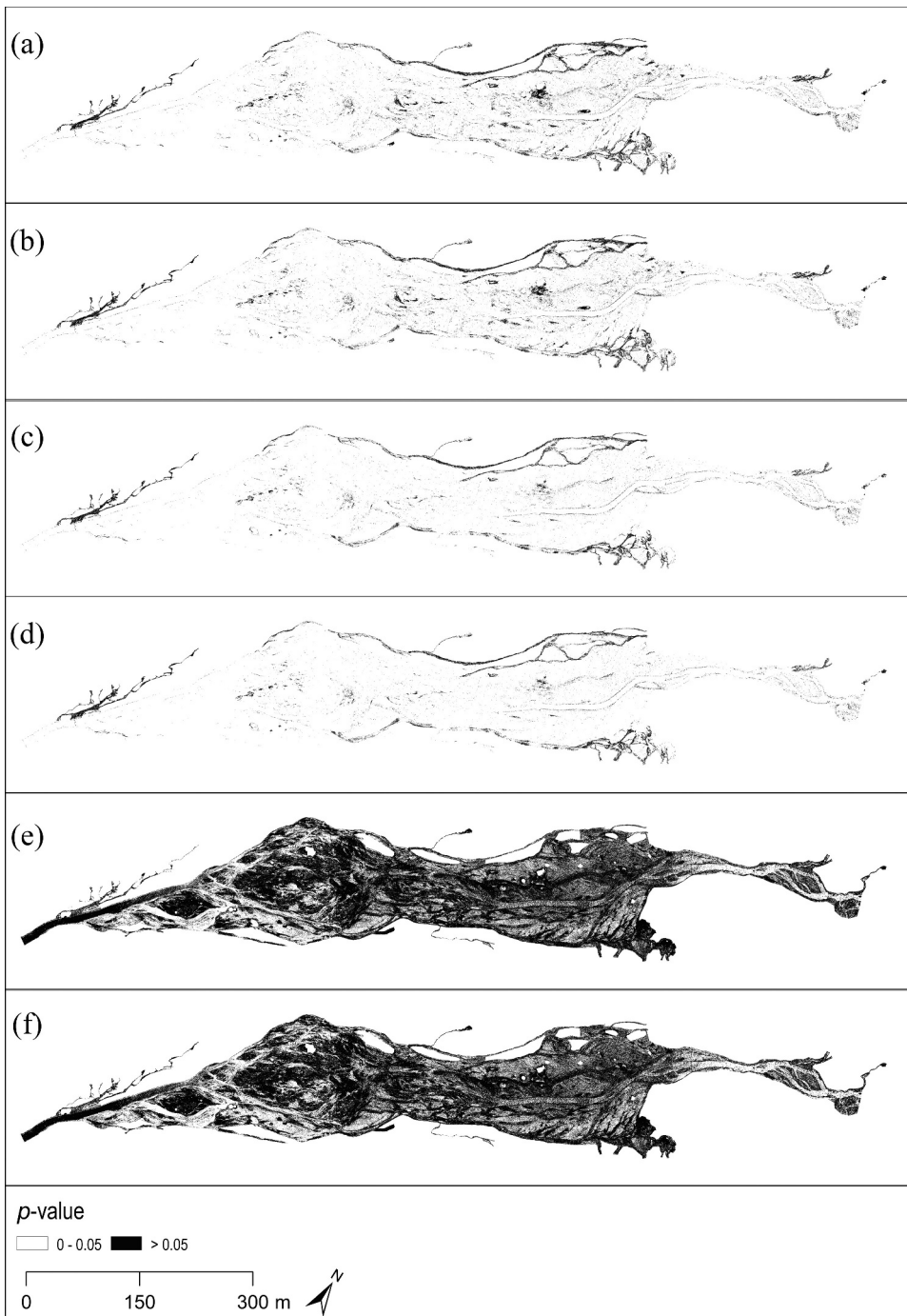


Figure 11. Maps of the probability that the time-series of occupation or non-occupation by biofilm is non-random ($p < 0.05$): a) the single dataset, b) the single-shadow dataset, c) the raw dataset, d) theraw-shadow dataset, e) the normalized dataset, and f) the normalized-shadow dataset.

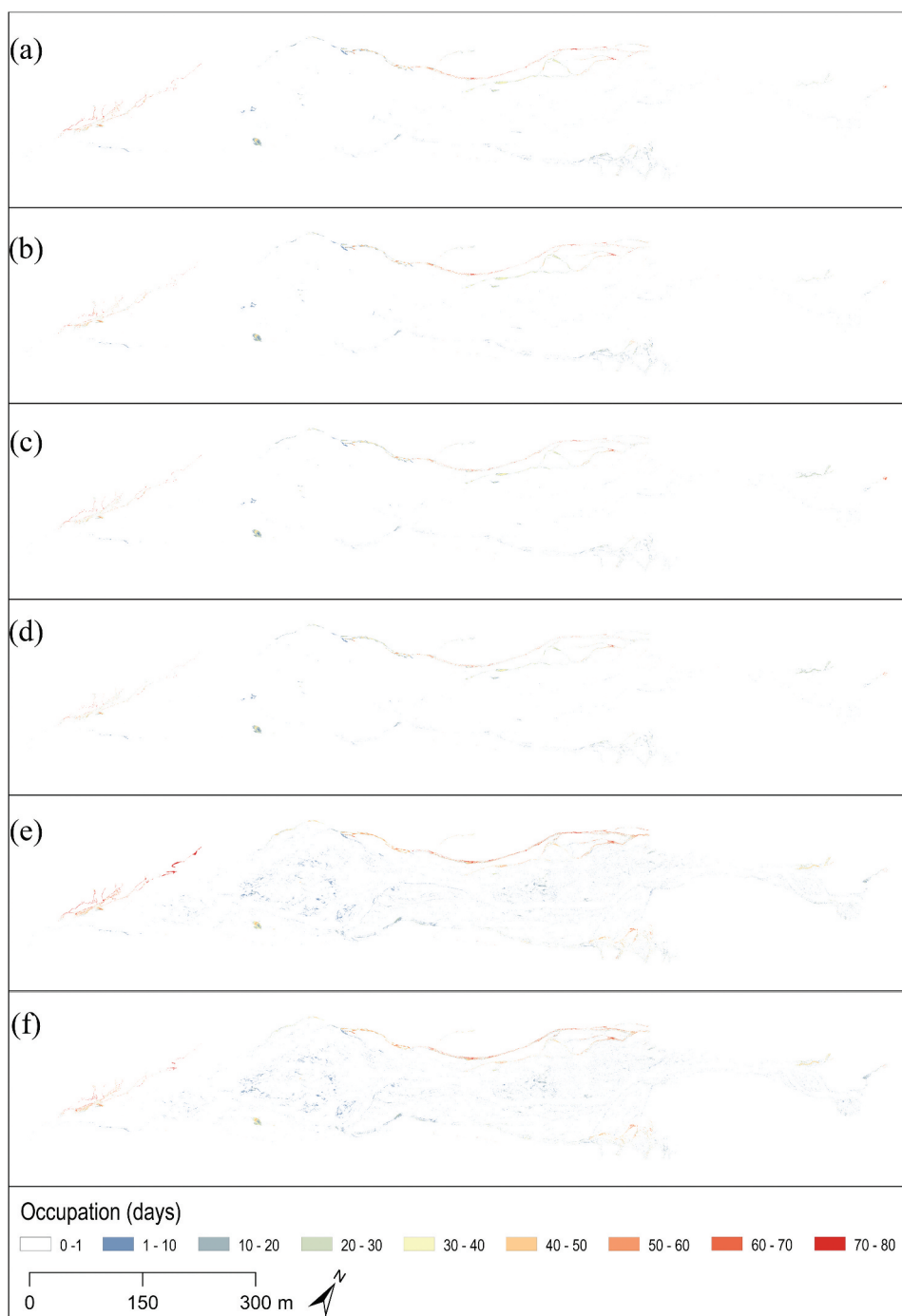


Figure 12. Occupation (in days) corrected for p -value of biofilms on the floodplain of the Glacier d'Otemma during the period 26 June to 13 September 2020. Occupation calculated from a) the single dataset, b) the single-shadow dataset, c) the raw dataset, d) the raw-shadow dataset, e) the normalized dataset, and f) the normalized-shadow dataset.

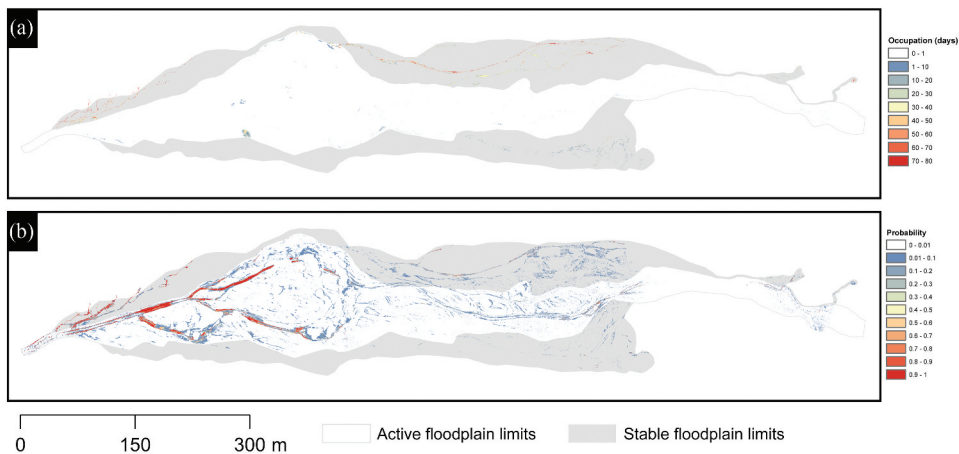


Figure 13. Season distribution of biofilm on the floodplain of the Glacier d'Otemma. a) Biofilm occupation map (single and p -value corrected), from 26 June to 13 September; b) Probability map for the 5 November.

overall biofilm extent mapped previously (Figure 9) was preserved in the new maps, although there was a generalized reduction of the biofilm extent at a threshold p -value = 0.05. Though such a threshold might be too strong, it produced maps where biofilm presence had a 95% probability of reflecting true biofilm dynamics. The normalized scenarios (Figure 12e,f) experienced the most important changes, with noise and systematic bias removed in large quantities from the new occupation maps, although some clusters and single pixels are still present. However, the overall extent resembled that of the more precise single and raw datasets (with and without shadow), with channels on the edges mapping the highest cumulative presence of biofilms.

3.7. Biofilm distribution in space and time

On the basis of the results in Section 3.6, we selected single corrected for p -value as the basis of the final biofilm maps. Being able to map the distribution of biofilms at the whole floodplain scale and at such a high temporal resolution allows investigation of the seasonal pattern of biofilm development. During the summer (Figure 13a) biofilms tend to develop in channels located on stable or less active zones. Our results demonstrate that occupation of biomass in the active floodplain is very uncommon during the melt-season, and most of the biomass accumulates in stable or less active channels that are disconnected from the destructive glacial braided stream. In November (Figure 13b), biofilm distributions appeared very different as compared to the summer, in fact pixels with high probabilities of being biofilms are found even in the active braidplain that during that time is occupied by a less destructive glacial stream. In more general terms, the distribution evolution shows that biofilms tend to develop in the channels located on stable zones from June through mid-September while they tend to migrate towards the main active floodplain from mid-September onwards (fall at such altitudes).

4. Discussion

4.1. Choice of logistic models

The choice of logistic models in this study produced very clear but different results. Within the band ratios and groups, the ExG and GLI significantly underperformed for the other indices analysed (Tables 3, 4 and 5). We assume that this finding is related to the nature of the benthic biofilms in the investigated forefield that were mainly reddish and/or brownish. In fact, both the ExG and GLI indices reduce the RGB information by using the green band as the principal component in the ratios and this may have biased the detection of red or brown patches. For instance, the GLI index (Louhaichi et al., 2001) was developed to detect wheat leaves and stems that have typically high green DNs compared to red (and blue). The NGRD, VARI, and RGRI ratios produced better results as compared to the ExG and GLI indices (Tables 3, 4 and 5). Similar to the GLI and ExG indices, the green band is a central component of the NGRD, VARI, and RGRI ratios, though the red band is more important which may explain their superior performance. Interestingly, the NGRD, VARI and RGRI indices had performances equal to the EXR, RCC, and KANA indices in Group 4 (Table 5), but this could be explained by the presence of snow over the floodplain than created a very dichotomous situation where only snow-free channels had a different spectral signature compared to the rest of the floodplain. Overall, the ExR, RCC, and KANA indices gave the best results (Tables 3, 4 and 5). This may be explained by the central role of the red band in the calculations that matched with most of the biofilm pixels used in the training/validation process. The positive role of the red band is well known in vegetation studies. In fact, most vegetation indices use the red band combined with the near-infrared to map vegetation (Gitelson et al., 2002).

Finally, the KANA index (Kawashima and Nakatani, 1998) was selected for the mapping of phototrophic biofilms because it showed the overall best performance across the tests reported here. It has been shown (Kawashima and Nakatani, 1998; Gitelson et al., 2002) that the use of the blue band can have a beneficial effect when phototrophically active pigments must be detected. Kawashima and Nakatani (1998) noted that the blue band had a nearly constant response to chlorophyll-*a* content regardless of meteorological conditions, while red (and green) a negative correlation, and the use of blue as a base value (i.e. $R-B$) reduces the probability of having biased values. We therefore assume that the KANA index had generally better performances because of the presence of mostly reddish and/or brownish biofilms and the fact that the blue band attenuated the effects of changing light conditions.

4.2. Orthomosaic normalization and biofilm maps

Although as part of our study we undertook single scene-by-scene calibration, this is labour intensive. Hence, we tested the use of a smaller number of reference images to develop the calibrations. It has been shown that multi-temporal image comparison can be difficult due to non-scene dependent changes (Schott et al., 1988; Du et al., 2002; Song and Woodcock, 2003; Liu et al., 2007; Bao et al., 2012) that can affect the reflectivity of ground objects, and hence create inter-scene differences that are not related to the signal that is of interest. The goal of the PIF normalization was to homogenize the set of

orthomosaics to resemble as much as possible our reference ones allowing the calibration of one single logistic model within each group: 14 July (groups 1 and 3), 26 July (Group 2) and 5 November (Group 4). The reference mosaics were converted into visible band ratios (Table 2) that have the advantage of reducing the RGB information to a point that is less sensitive to the solar radiation (Woebbecke et al., 1995; Kawashima and Nakatani, 1998; Cheng et al., 2001).

Despite a generalized RMSE reduction after the PIF normalization (Figure 3), the relative radiometric normalization method showed relatively mixed results whether considered in terms of the validation results (Figure 7) and the impacts on the occupation maps (Figures 9 and 10). Individual scenes had variable differences in their red, green and blue digital numbers before normalization and normalization was variable in the extent to which these differences could be reduced (Figure 3). Differences in the covariance of scene and reference digital numbers (compare Figures 4, 5 and 6) reflect this variable performance. We think it can be traced to three main reasons. First, it is preferable to select artificial PIFs (e.g. roofs, streets) to perform a radiometric normalization (Schott et al., 1988), but these only partially available here for the 55% of PIFs that were ground control points. These covered a restricted spectral range as they were black and yellow and were also distributed to optimize the SfM photogrammetric processing and not for the need of spectral normalization. Second, when shadows were present over the floodplain (e.g. Figure 4b), they modified the reflectivity of the ground and those PIFs occurring in a shadowed portion of the floodplain had very different values compared to those of the reference orthomosaics. This increased point dispersion in the model (e.g. Figure 4a). Shadows could only be corrected at the scale of the micro-topography due to unknown cloud cover. Third, it took 3.5 hours to image the complete floodplain, and when the floodplain was imaged was conditioned by the need to survey at low flows when as little of the floodplain as possible was inundated by turbid water. PIF normalization works well with satellites (Schott et al., 1988; Liu et al., 2007) that instantaneously image large areas, which by definition contain no spatial signature of temporally evolving light conditions. This is partly reflected in differences between groups. Group 1 contained data from close to the summer solstice when the survey had to be completed before the sun had risen above local mountains due to rapid water level rise mid-morning. Group 3 contained data at the end of the summer when the river stage rose later and so the flight could be undertaken in fully light conditions. Both had more homogeneous lighting and the normalization was needed less (Group 3, Figure 3) or was more effective (Group 1, Figure 3) than for Group 2. Commonly, during Group 2 image acquisition the floodplain went from being fully shaded to being fully exposed to sunlight.

The negative impacts of normalization were reflected in a general overestimation of biofilm extent as reflected in the occupation and OoD maps (Figure 9e,f and 10d,e). This was partly reflected in the validation statistics (Figure 7) which suggested very mixed results, even degrading statistics markedly and notably for the Group 2 data. The overestimation reflects the problem that re-assembly of the single normalized bands into an RGB image can lead to a colour tone deterioration (Figure 4b), potentially caused by a new predominance of one of the three bands over the others. Here, the PIF normalization increased the DN_s of our orthomosaics, then the index values and resulted in

a generalized and systematic exceedance of the reference thresholds (i.e. 0.5 probability threshold) when occupation maps were generated. Notably, red DN_s (e.g. wet sediments) became red dominated and so mapped as being biofilms.

This would question whether normalization of the sort used here was appropriate and perhaps suggests the need for a more physically based model-informed spectral correction (e.g. one that could be time-dependent when ambient lighting changes during data collection). The raw datasets were actually more consistent with the single image datasets. However, they had a tendency to underestimate biofilm extent (Figure 10b,c). This is likely because the reference thresholds from the logistic model were too strong for most of the dates such that less biofilm was detected when the reference 0.5-probability limit was applied.

The single image calibration models produced the cleanest probability and occupation maps (Figure 9a,b). This is not surprising as we trained a logistic model for each orthomosaic, resulting in models most suitable for the given situation (i.e. adapted threshold). They performed better in capturing the lighting characteristics of each scene provided there is reasonable lighting homogeneity within that scene. The reason for the multi-hour UAV flight time was to secure the high resolution needed to capture biofilm development for small scales over a large spatial extent. Thus, for these kinds of surveys, lighting is likely to be an issue and, at least until a more advanced normalization process is developed, it implies that more labour-intensive scene-specific calibration models are required.

We also evaluated the extent to which micro-topography shadows had an impact on our classifications. Micro-topography shadows were successfully detected and masked through segmentation of the potential solar radiation models (Kumar et al., 1997). The DEM resolution was sufficiently fine that in some cases moving surfaces (e.g. water) were mapped as having relief that created shadow (Figure 8c). Such artefacts occurred where biofilm either cannot develop or be visible due to the highly suspended sediment load. Although the shadow correction had a clearly beneficial effect on removing zones that were not biofilms, there were some zones where masking micro-topography shadows excluded also pixels that were likely to be true biofilms and the OoD between the single and single-shadow datasets (Figure 10a) demonstrated this. These were commonly related to pebbles and boulders located within and/or on the edges of channels that created shadowed pixels that were subsequently masked and excluded from calculation in the occupation maps. The positive contribution of the micro-topography models was limited to those pixels located on the transitions between steep banks and water surfaces that likely caused spectral confusion in our models.

Finally, the runs test provided a biologically informed statistical way to filter our occupations maps in which the pixels with p -value >0.05 were discarded in occupation calculations. In the single and raw datasets (Figures 11(a–d)) and Figure 12(a–d)), this might have excluded some pixels that were likely to reflect true biofilm dynamics (e.g. biofilms in side channels), but ensured that what was eventually mapped had a 95% probability of reflecting true dynamics (either presence, presence/destruction, or absence). The normalized dataset quality (Figure 12e,f) was enhanced as compared to previous results (Figure 9e,f), but some of the systematic bias caused by the normalization process was still present.

Our results suggested that phototrophic biofilms can be mapped through the combination of very low-cost UAVs and RGB cameras, but attention must be paid to lighting, hence the calibration of a scene-to-scene model (i.e. single) and using a biologically informed statistical feature appeared to be the most well suited for the range of conditions we encountered during the data collection.

4.3. Seasonal distribution of phototrophic biofilms and implications

Being able to map biofilm distributions and cumulative biofilm presence at high temporal and spatial resolutions provides important insights into benthic habitat functioning and how it responds to and co-evolves with external stressors. It is well known that glacial forefields are harsh environments due to their highly dynamic and unstable nature (Marren 2005; Heckmann et al., 2016). Bakker et al., (2019) demonstrated that during the summer glacial streams continuously rework their accommodation spaces (i.e. floodplains) by erosion and deposition processes, resulting in low rates of environmental stability. This creates a disturbance-dominated regime that can influence biofilm development and/or survival, and is mainly controlled by the glacial-driven flow hydraulics. Bed load (i.e. bed instability) may impede biofilm development (Uehlinger et al., 1998; Uehlinger et al., 2002, 2010; Rott et al., 2006), while high shear stresses may scour developed communities (Biggs and Close, 1989; Horner et al., 1990; Biggs and Thomsen, 1995; Cullis et al., 2014). The high suspended load may be responsible for biofilm abrasion (Horner and Welch, 1981; Horner et al., 1990; Francoeur and Biggs, 2006; Luce et al., 2010, 2013) but also limit the access to the photosynthetically active radiation (Uehlinger et al., 2010). This explains why biofilm biomass is low during the melt-season (Uehlinger et al., 2002, 2010), but reaches two maxima during spring and fall, known as 'windows of opportunity' (see Uehlinger et al., 2002, 2010), because environmental conditions are less harsh (i.e. low discharge, low turbidity, and low or no bedload). From our maps (Figure 12), it is not possible to retrieve biofilm biomass directly, but our results tend to confirm the assumptions of Uehlinger and colleagues in relation to an autumn window. Biofilm presence was restricted to stable and water-fed terraces from June through late August. As the rate of morphodynamic change reduced from late August onwards, biofilm extent increased and presumably reached its highest mapped surface in November when the gelatinous dark-brown *Hydrurus foetidus* (Rott et al., 2006; Uehlinger et al., 2010) colonized extensive areas, including the turbid, most morphodynamically active main stream.

5. Conclusion

Here, we present a framework for mapping biofilm distributions by applying logistic regression to visible band ratios using UAV-based imagery processed using SfM-MVS photogrammetry. We demonstrated that with mapping at high frequency (daily) and spatial (cm) resolution, there is no need for expensive multi- or even hyper-spectral sensors in order to obtain valuable information on biofilm dynamics. Use of a suitable visible band ratio would be enough in most mapping scenarios due to the different colours of biofilms compared to the un-colonized substratum and these are retrievable in the visible range. We applied a basic linear normalization process to normalize

our orthomosaics. The effects of this were not conclusive and this was primarily because of non-homogeneous light conditions that caused considerable scatter in the training relations, but also meant that a linear correction was not always appropriate. A biologically-informed filter was particularly effective at removing points that would otherwise have been mapped as biofilms. Despite these issues, we were able to generate a time-series of distribution maps of an Alpine glacial floodplain that covers an entire melting season, from June to September. These maps will allow new insights on how biofilms develop and co-evolve in the harsh environment of a glacial forefield.

Acknowledgements

We would like to acknowledge all the people that helped us in collecting the UAV images during the Otemma field campaign of summer 2020, in particular: Adrijan Seltaj, Frédéric Lardet, Margaux Hoffman, Alissa Pott, Lara Mercier, Gwendoline Perritaz, Boris Ouvry, Isabel Herr, Pierre Hauptmann, Valentine Grünwald and Valentin Cina-Colman.

Disclosure statement

No potential conflict of interest was reported by the author(s).

Funding

This study is supported by Swiss National Science Foundation Sinergia grant CRSII5_180241 ENSEMBLE awarded to T. I. Battin, S. N. Lane, M. Lever and P. Wilmes; Schweizerischer Nationalfonds zur Förderung der Wissenschaftlichen Forschung [CRSII5_180241]

ORCID

Matteo Roncoroni  <http://orcid.org/0000-0001-6957-6225>

Davide Mancini  <http://orcid.org/0000-0003-4022-4351>

Tyler J. Kohler  <http://orcid.org/0000-0001-5137-4844>

Stuart N. Lane  <http://orcid.org/0000-0002-6077-6076>

Data availability statement

Data available at <https://doi.org/10.5281/zenodo.6598305>

References

- Adamsen, F. J., P. J. Pinter, E. M. Barnes, R. L. LaMorte, G. W. Wall, S. W. Leavitt, and B. A. Kimball. 1999. "Measuring Wheat Senescence with a Digital Camera." *Crop Science* 39 (3): crops1999.0011183X003900030019x. doi:10.2135/cropsci1999.0011183X003900030019x.
- Bakker, M., G. Antoniazza, E. Odermatt, and S. N. Lane. 2019. "Morphological Response of an Alpine Braided Reach to Sediment-laden Flow Events." *Journal of Geophysical Research: Earth Surface* 124 (5): 1310–1328. doi:<https://doi.org/10.1029/2018JF004811>.

- Bao, N., A. M. Lechner, A. Fletcher, D. Mulligan, A. Mellor, and Z. Bai. 2012. "Comparison of Relative Radiometric Normalization Methods Using Pseudo-Invariant Features for Change Detection Studies in Rural and Urban Landscapes." *Journal of Applied Remote Sensing* 6 (1): 063578. doi:10.1117/1.JRS.6.063578.
- Battin, T. J., L. A. Kaplan, J. Denis Newbold, and C. M. E. Hansen. 2003. "Contributions of Microbial Biofilms to Ecosystem Processes in Stream Mesocosms." *Nature* 426 (6965): 439–442. doi:10.1038/nature02152.
- Battin, T. J., L. A. Kaplan, S. Findlay, C. S. Hopkinson, E. Marti, A. I. Packman, J. D. Newbold, and F. Sabater. 2008. "Biophysical Controls on Organic Carbon Fluxes in Fluvial Networks." *Nature Geoscience* 1 (2): 95–100. doi:10.1038/ngeo101.
- Battin, T. J., K. Besemer, M. M. Bengtsson, A. M. Romani, and A. I. Packmann. 2016. "The Ecology and Biogeochemistry of Stream Biofilms." *Nature Reviews: Microbiology* 14 (4): 251–263. doi:10.1038/nrmicro.2016.15.
- Benyoucef, I., E. Blandin, A. Lerouxel, B. Jesus, P. Rosa, V. Méléder, P. Launeau, and L. Barillé. 2014. "Microphytobenthos Interannual Variations in a North-European Estuary (Loire Estuary, France) Detected by Visible-Infrared Multispectral Remote Sensing." *Estuarine, Coastal and Shelf Science* 136: 43–52. doi:10.1016/j.ecss.2013.11.007.
- Biggs, B. J. F. and M. E. Close. 1989. "Periphyton Biomass Dynamics in Gravel Bed Rivers: The Relative Effects of Flows and Nutrients." *Freshwater Biology* 22 (2): 209–231. doi:10.1111/j.1365-2427.1989.tb01096.x.
- Biggs, B. J. F. and H. A. Thomsen. 1995. "Disturbance of Stream Periphyton by Perturbations in Shear Stress: Time to Structural Failure and Differences in Community Resistance." *Journal of Phycology* 31 (2): 233–241. doi:10.1111/j.0022-3646.1995.00233.x.
- Bioucas-Dias, J. M., A. Plaza, G. Camps-Valls, P. Scheunders, N. Nasrabadi, and J. Chanussot. 2013. "Hyperspectral Remote Sensing Data Analysis and Future Challenges." *IEEE Geoscience and Remote Sensing Magazine* 1 (2): 6–36. doi:10.1109/MGRS.2013.2244672.
- Brückner, M. Z. M., C. Schwarz, G. Coco, A. Baar, M. Boechat Albernaz, and M. G. Kleinhans. 2021. "Benthic Species as Mud Patrol—modelled Effects of Bioturbators and Biofilms on Large-Scale Estuarine Mud and Morphology." *Earth Surface Processes and Landforms* 46 (6): 1128–1144. doi:10.1002/esp.5080.
- Carbonneau, P. E., S. N. Lane, and N. E. Bergeron. 2004. "Catchment-Scale Mapping of Surface Grain Size in Gravel Bed Rivers Using Airborne Digital Imagery: MAPPING GRAIN SIZE in GRAVEL BED RIVERS." *Water Resources Research* 40 (7). doi:10.1029/2003WR002759.
- Chabot, D., C. Dillon, A. Shemrock, N. Weissflog, and E. Sager. 2018. "An Object-Based Image Analysis Workflow for Monitoring Shallow-Water Aquatic Vegetation in Multispectral Drone Imagery." *ISPRS International Journal of Geo-Information* 7 (8): 294. doi:10.3390/ijgi7080294.
- Cheng, H. D., X. H. Jiang, Y. Sun, and J. Wang. 2001. "Color Image Segmentation: Advances and Prospects." *Pattern Recognition* 34 (12): 2259–2281. doi:10.1016/S0031-3203(00)00149-7.
- Chicco, D. and G. Jurman. 2020. "The Advantages of the Matthews Correlation Coefficient (MCC) Over F1 Score and Accuracy in Binary Classification Evaluation." *BMC Genomics* 21 (1): 6. doi:10.1186/s12864-019-6413-7.
- Combe, J.-P., P. Launeau, V. Carrère, D. Despan, V. Méléder, L. Barillé, and C. Sotin. 2005. "Mapping Microphytobenthos Biomass by Non-Linear Inversion of Visible-Infrared Hyperspectral Images." *Remote Sensing of Environment* 98 (4): 371–387. doi:10.1016/j.rse.2005.07.010.
- Costerton, J. W., K. J. Cheng, G. G. Geesey, T. I. Ladd, J. C. Nickel, M. Dasgupta, and T. J. Marrie. 1987. "Bacterial Biofilms in Nature and Disease." *Annual Review of Microbiology* 41 (1): 435–464. doi:10.1146/annurev.mi.41.100187.002251.
- Costerton, J. W., Z. Lewandowski, D. E. Caldwell, D. R. Korber, and H. M. Lappin-Scott. 1995. "Microbial Biofilms." *Annual Review of Microbiology* 49 (1): 711–745. doi:10.1146/annurev.mi.49.100195.003431.
- Cullis, J. D. S., L. F. Stanish, and D. M. McKnight. 2014. "Diel Flow Pulses Drive Particulate Organic Matter Transport from Microbial Mats in a Glacial Meltwater Stream in the McMurdo Dry Valleys." *Water Resources Research* 50 (1): 86–97. doi:10.1002/2013WR014061.

- Dietrich, J. T. 2017. "Bathymetric Structure-From-Motion: Extracting Shallow Stream Bathymetry from Multi-View Stereo Photogrammetry." *Earth Surface Processes and Landforms* 42 (2): 355–364. doi:10.1002/esp.4060.
- Du, Y., P. M. Teillet, and J. Cihlar. 2002. "Radiometric Normalization of Multitemporal High-Resolution Satellite Images with Quality Control for Land Cover Change Detection." *Remote Sensing of Environment* 82 (1): 123–134. doi:10.1016/S0034-4257(02)00029-9.
- Fang, H., Q. Shang, M. Chen, and G. He. 2014. "Changes in the Critical Erosion Velocity for Sediment Colonized by Biofilm." *Sedimentology* 61 (3): 648–659. doi:10.1111/sed.12065.
- Flemming, H.-C. and J. Wingender. 2010. "The Biofilm Matrix." *Nature Reviews: Microbiology* 8 (9): 623–633. doi:10.1038/nrmicro2415.
- Flemming, H.-C. and S. Wuertz. 2019. "Bacteria and Archaea on Earth and Their Abundance in Biofilms." *Nature Reviews: Microbiology* 17 (4): 247–260. doi:10.1038/s41579-019-0158-9.
- Flynn, K. and S. Chapra. 2014. "Remote Sensing of Submerged Aquatic Vegetation in a Shallow Non-Turbid River Using an Unmanned Aerial Vehicle." *Remote Sensing* 6 (12): 12815–12836. doi:10.3390/rs61212815.
- Fonstad, M. A., J. T. Dietrich, B. C. Courville, J. L. Jensen, and P. E. Carbonneau. 2013. "Topographic Structure from Motion: A New Development in Photogrammetric Measurement." *Earth Surface Processes and Landforms* 38 (4): 421–430. doi:10.1002/esp.3366.
- Francoeur, S. N. and B. J. F. Biggs. 2006. "Short-Term Effects of Elevated Velocity and Sediment Abrasion on Benthic Algal Communities." *Hydrobiologia* 561 (1): 59–69. doi:10.1007/s10750-005-1604-4.
- Gerbersdorf, S. U., W. Manz, and D. M. Paterson. 2008. "The Engineering Potential of Natural Benthic Bacterial Assemblages in Terms of the Erosion Resistance of Sediments." *FEMS Microbiology Ecology* 66 (2): 282–294. doi:10.1111/j.1574-6941.2008.00586.x.
- Gerbersdorf, S. U., B. Westrich, and D. M. Paterson. 2009. "Microbial Extracellular Polymeric Substances (EPS) in Fresh Water Sediments." *Microbial Ecology* 58 (2): 334–349. doi:10.1007/s00248-009-9498-8.
- Gerbersdorf, S. U. and S. Wieprecht. 2015. "Biostabilization of Cohesive Sediments: Revisiting the Role of Abiotic Conditions, Physiology and Diversity of Microbes, Polymeric Secretion, and Biofilm Architecture." *Geobiology* 13 (1): 68–97. doi:10.1111/gbi.12115.
- Gitelson, A. A., Y. J. Kaufman, R. Stark, and D. Rundquist. 2002. "Novel Algorithms for Remote Estimation of Vegetation Fraction." *Remote Sensing of Environment* 80 (1): 76–87. doi:10.1016/S0034-4257(01)00289-9.
- Harrison L R, Legleiter C J, Overstreet B T, Bell T W and Hannon J. (2020). Assessing the potential for spectrally based remote sensing of salmon spawning locations. *River Res Applic*, 36(8), 1618–1632. doi:10.1002/rra.3690
- Heckmann, T., S. McColl, and D. Morche. 2016. "Retreating Ice: Research in Pro-Glacial Areas Matters." *Earth Surface Processes and Landforms* 41 (2): 271–276. doi:10.1002/esp.3858.
- Horner, R. R. and E. B. Welch. 1981. "Stream Periphyton Development in Relation to Current Velocity and Nutrients." *Canadian Journal of Fisheries and Aquatic Sciences* 38 (4): 449–457. doi:10.1139/f81-062.
- Horner, R. R., E. B. Welch, M. R. Seeley, and J. M. Jacoby. 1990. "Responses of Periphyton to Changes in Current Velocity, Suspended Sediment and Phosphorus Concentration." *Freshwater Biology* 24 (2): 215–232. doi:10.1111/j.1365-2427.1990.tb00704.x.
- James, M. R. and S. Robson. 2014. "Mitigating Systematic Error in Topographic Models Derived from UAV and Ground-Based Image Networks." *Earth Surface Processes and Landforms* 39 (10): 1413–1420. doi:10.1002/esp.3609.
- James, M. R., S. Robson, S. D’Oleire-Oltmanns, and U. Niethammer. 2017. "Optimising UAV Topographic Surveys Processed with Structure-From-Motion: Ground Control Quality, Quantity and Bundle Adjustment." *Geomorphology* 280: 51–66. doi:10.1016/j.geomorph.2016.11.021.
- James, M. R., G. Antoniazza, S. Robson, and S. N. Lane. 2020. "Mitigating Systematic Error in Topographic Models for Geomorphic Change Detection: Accuracy, Precision and Considerations Beyond Off-nadir Imagery." *Earth Surface Processes and Landforms* 45 (10): 2251–2271. doi:10.1002/esp.4878.

- Jones, C. G., J. H. Lawton, and M. Shachak. 1994. "Organisms as Ecosystem Engineers." *Oikos* 69 (3): 373–386. JSTOR. doi:10.2307/3545850.
- Kawashima, S. and M. Nakatani. 1998. "An Algorithm for Estimating Chlorophyll Content in Leaves Using a Video Camera." *Annals of Botany* 81 (1): 49–54. doi:10.1006/anbo.1997.0544.
- Kazemipour, F., P. Launeau, and V. Méléder. 2012. "Microphytobenthos Biomass Mapping Using the Optical Model of Diatom Biofilms: Application to Hyperspectral Images of Bourgneuf Bay." *Remote Sensing of Environment* 127: 1–13. doi:10.1016/j.rse.2012.08.016.
- Kislik, C., I. Dronova, and M. Kelly. 2018. "Uavs in Support of Algal Bloom Research: A Review of Current Applications and Future Opportunities." *Drones* 2 (4): 35. doi:10.3390/drones2040035.
- Kislik, C., L. Genzoli, A. Lyons, and M. Kelly. 2020. "Application of UAV Imagery to Detect and Quantify Submerged Filamentous Algae and Rooted Macrophytes in a Non-Wadeable River." *Remote Sensing* 12 (20): 3332. doi:10.3390/rs12203332.
- Kumar, L., A. K. Skidmore, and E. Knowles. 1997. "Modelling Topographic Variation in Solar Radiation in a GIS Environment." *International Journal of Geographical Information Science* 11 (5): 475–497. doi:10.1080/136588197242266.
- Lamberti, G. A. 1996. "The Role of Periphyton in Benthic Food Webs." In *Algal Ecology*, 533–572. Elsevier. doi:10.1016/B978-012668450-6/50046-1.
- Lane, S. N., A. Gentile, and L. Goldenschue. 2020. "Combining UAV-Based SfM-MVS Photogrammetry with Conventional Monitoring to Set Environmental Flows: Modifying Dam Flushing Flows to Improve Alpine Stream Habitat." *Remote Sensing* 12 (23): 3868. doi:10.3390/rs12233868.
- Launeau, P., V. Méléder, C. Verpoorter, L. Barillé, F. Kazemipour-Ricci, M. Giraud, B. Jesus, and E. Le Menn. 2018. "Microphytobenthos Biomass and Diversity Mapping at Different Spatial Scales with a Hyperspectral Optical Model." *Remote Sensing* 10 (5): 716. doi:10.3390/rs10050716.
- Liu, Y., T. Yano, S. Nishiyama, and R. Kimura. 2007. "Radiometric Correction for Linear Change-detection Techniques: Analysis in Bi-temporal Space." *International Journal of Remote Sensing* 28 (22): 5143–5157. doi:10.1080/01431160701268954.
- Louhaichi, M., M. M. Borman, and D. E. Johnson. 2001. "Spatially Located Platform and Aerial Photography for Documentation of Grazing Impacts on Wheat." *Geocarto International* 16 (1): 65–70. doi:10.1080/10106040108542184.
- Luce, J. J., A. Cattaneo, and M. F. Lapointe. 2010. "Spatial Patterns in Periphyton Biomass After Low-Magnitude Flow Spates: Geomorphic Factors Affecting Patchiness Across Gravel–cobble Riffles." *Journal of the North American Benthological Society* 29 (2): 614–626. doi:10.1899/09-059.1.
- Luce, J. J., M. F. Lapointe, A. G. Roy, and D. B. Ketterling. 2013. "The Effects of Sand Abrasion of a Predominantly Stable Stream Bed on Periphyton Biomass Losses: Effects of Sand Abrasion of a Stable Stream Bed on Periphyton Biomass Losses." *Ecohydrology* 6 (4): 689–699. doi:10.1002/eco.1332.
- Mancini, D. and S. N. Lane. 2020. "Changes in Sediment Connectivity Following Glacial Debuttressing in an Alpine Valley System." *Geomorphology* 352: 106987. doi:10.1016/j.geomorph.2019.106987.
- Mao, W., Y. Wang, and Y. Wang. 2003. "Real-Time Detection of Between-Row Weeds Using Machine Vision." 2003, Las Vegas, NV July 27-30, 2003. 2003, Las Vegas, NV, July 27-30. 10.13031/2013.15381
- Marcus, W. A. and M. A. Fonstad. 2008. "Optical Remote Mapping of Rivers at Sub-Meter Resolutions and Watershed Extents." *Earth Surface Processes and Landforms* 33 (1): 4–24. doi:10.1002/esp.1637.
- Marren, P. M. 2005. "Magnitude and Frequency in Proglacial Rivers: A Geomorphological and Sedimentological Perspective." *Earth-Science Reviews* 70 (3): 203–251. doi:10.1016/j.earscirev.2004.12.002.
- Méléder, V., P. Launeau, L. Barillé, and Y. Rincé. 2003. "Microphytobenthos Assemblage Mapping by Spatial Visible-Infrared Remote Sensing in a Shellfish Ecosystem." *Comptes Rendus Biologies* 326 (4): 377–389. doi:10.1016/S1631-0691(03)00125-2.
- Meyer, G. E., T. Mehta, M. F. Kocher, D. A. Mortensen, and A. Samal. 1998. "Textural Imaging and Discriminant Analysis for Distinguishing weeds for Spot Spraying." *Transactions of the ASAE* 41 (4): 1189–1197. doi:10.13031/2013.17244.

- Meyer, G. E. and J. C. Neto. 2008. "Verification of Color Vegetation Indices for Automated Crop Imaging Applications." *Computers and Electronics in Agriculture* 63 (2): 282–293. doi:10.1016/j.compag.2008.03.009.
- Miller, H. R. and S. N. Lane. 2019. "Biogeomorphic Feedbacks and the Ecosystem Engineering of Recently Deglaciated Terrain." *Progress in Physical Geography: Earth and Environment* 43 (1): 24–45. doi:10.1177/0309133318816536.
- Neumeier, U., C. H. Lucas, and M. Collins. 2006. "Erodibility and Erosion Patterns of Mudflat Sediments Investigated Using an Annular Flume." *Aquatic Ecology* 40 (4): 543–554. doi:10.1007/s10452-004-0189-8.
- Power, S. N., M. R. Salvatore, E. R. Sokol, L. F. Stanish, and J. E. Barrett. 2020. "Estimating Microbial Mat Biomass in the McMurdo Dry Valleys, Antarctica Using Satellite Imagery and Ground Surveys." *Polar Biology* 43 (11): 1753–1767. doi:10.1007/s00300-020-02742-y.
- Roncoroni, M., J. Brandani, T. I. Battin, and S. N. Lane. 2019. "Ecosystem Engineers: Biofilms and the Ontogeny of Glacier Floodplain Ecosystems." *Wiley Interdisciplinary Reviews: Water* 6 (6). doi:10.1002/wat2.1390.
- Roncoroni, M. and S. N. Lane. 2019. "A framework for using small Unmanned Aircraft Systems (sUASs) and SfM photogrammetry to detect salmonid redds." *Ecological Informatics* 53: 100976. doi:10.1016/j.ecoinf.2019.100976.
- Rott, E., M. Cantonati, L. Füreder, and P. Pfister. 2006. "Benthic Algae in High Altitude Streams of the Alps – a Neglected Component of the Aquatic Biota." *Hydrobiologia* 562 (1): 195–216. doi:10.1007/s10750-005-1811-z.
- Saberioon, M. M., M. S. M. Amin, A. R. Anuar, A. Gholizadeh, A. Wayayok, and S. Khairunniza-Bejo. 2014. "Assessment of Rice Leaf Chlorophyll Content Using Visible Bands at Different Growth Stages at Both the Leaf and Canopy Scale." *International Journal of Applied Earth Observation and Geoinformation* 32: 35–45. doi:10.1016/j.jag.2014.03.018.
- Salvatore, M. R., S. R. Borges, J. E. Barrett, E. R. Sokol, L. F. Stanish, S. N. Power, and P. Morin. 2020. "Remote Characterization of Photosynthetic Communities in the Fryxell Basin of Taylor Valley, Antarctica." *Antarctic Science* 32 (4): 255–270. doi:10.1017/S0954102020000176.
- Schott, J. R., C. Salvaggio, and W. J. Volchok. 1988. "Radiometric Scene Normalization Using Pseudoinvariant Features." *Remote Sensing of Environment* 26 (1): 1–16. doi:10.1016/0034-4257(88)90116-2.
- Schroeder, T. A., W. B. Cohen, C. Song, M. J. Canty, and Z. Yang. 2006. "Radiometric Correction of Multi-Temporal Landsat Data for Characterization of Early Successional Forest Patterns in Western Oregon." *Remote Sensing of Environment* 103 (1): 16–26. doi:10.1016/j.rse.2006.03.008.
- Song, C. and C. E. Woodcock. 2003. "Monitoring Forest Succession with Multitemporal Landsat Images: Factors of Uncertainty." *IEEE Transactions on Geoscience and Remote Sensing* 41 (11): 2557–2567. doi:10.1109/TGRS.2003.818367.
- Song, B. and K. Park. 2020. "Detection of Aquatic Plants Using Multispectral UAV Imagery and Vegetation Index." *Remote Sensing* 12 (3): 387. doi:10.3390/rs12030387.
- Su, T.-C. and H.-T. Chou. 2015. "Application of Multispectral Sensors Carried on Unmanned Aerial Vehicle (UAV) to Trophic State Mapping of Small Reservoirs: A Case Study of Tain-Pu Reservoir in Kinmen, Taiwan." *Remote Sensing* 7 (8): 10078–10097. doi:10.3390/rs70810078.
- Taddia, Y., P. Russo, S. Lovo, and A. Pellegrinelli. 2020. "Multispectral UAV Monitoring of Submerged Seaweed in Shallow Water." *Applied Geomatics* 12 (1): 19–34. doi:10.1007/s12518-019-00270-x.
- Tamminga, A., C. Hugenholtz, B. Eaton, and M. Lapointe. 2015. "Hyperspatial Remote Sensing of Channel Reach Morphology and Hydraulic Fish Habitat Using an Unmanned Aerial Vehicle (UAV): A First Assessment in the Context of River Research and Management: REMOTE SENSING USING UAVS." *River Research and Applications* 31 (3): 379–391. doi:10.1002/rra.2743.
- Tucker, C. J. 1979. "Red and Photographic Infrared Linear Combinations for Monitoring Vegetation." *Remote Sensing of Environment* 8 (2): 127–150. doi:10.1016/0034-4257(79)90013-0.
- Uehlinger, U., R. Zah, and H. Bürgi. 1998. "The Val Roseg Project: Temporal and Spatial Patterns of Benthic Algae in an Alpine Stream Ecosystem Influenced by Glacier Runoff." *IAHS Publ* 248: 419–424.

- Uehlinger, U., K. Tockner, and F. Malard. 2002. "Ecological Windows in Glacial Stream Ecosystems." *Eawag News [Engl. Ed.]* 54: 20–21.
- Uehlinger, U., C. T. Robinson, M. Hieber, and R. Zah. 2010. "The Physico-Chemical Habitat Template for Periphyton in Alpine Glacial Streams Under a Changing Climate." *Hydrobiologia* 657 (1): 107–121. doi:[10.1007/s10750-009-9963-x](https://doi.org/10.1007/s10750-009-9963-x).
- Westoby, M. J., J. Brasington, N. F. Glasser, M. J. Hambrey, and J. M. Reynolds. 2012. "'Structure-From-Motion' Photogrammetry: A Low-Cost, Effective Tool for Geoscience Applications." *Geomorphology* 179: 300–314. doi:[10.1016/j.geomorph.2012.08.021](https://doi.org/10.1016/j.geomorph.2012.08.021).
- Woebbecke, D. M., G. E. Meyer, K. Von Bargen, and D. A. Mortensen. 1995. "Color Indices for Weed Identification Under Various Soil, Residue, and Lighting Conditions." *Transactions of the ASAE* 38 (1): 259–269. doi:[10.13031/2013.27838](https://doi.org/10.13031/2013.27838).
- Woodget, A. S., P. E. Carbonneau, F. Visser, and I. P. Maddock. 2015. "Quantifying Submerged Fluvial Topography Using Hyperspatial Resolution UAS Imagery and Structure from Motion Photogrammetry." *Earth Surface Processes and Landforms* 40 (1): 47–64. doi:[10.1002/esp.3613](https://doi.org/10.1002/esp.3613).
- Woodget, A. S. and R. Austrums. 2017. "Subaerial Gravel Size Measurement Using Topographic Data Derived from a UAV-SfM Approach." *Earth Surface Processes and Landforms* 42 (9): 1434–1443. doi:[10.1002/esp.4139](https://doi.org/10.1002/esp.4139).
- Xu, F., Z. Gao, X. Jiang, W. Shang, J. Ning, D. Song, and J. Ai. 2018. "A UAV and S2A Data-Based Estimation of the Initial Biomass of Green Algae in the South Yellow Sea." *Marine Pollution Bulletin* 128: 408–414. doi:[10.1016/j.marpolbul.2018.01.061](https://doi.org/10.1016/j.marpolbul.2018.01.061).